Phenomenology of Supernova Neutrinos, Spatial Event Reconstruction, and Scintillation Light Yield Measurements for the Liquid-Scintillator Detector LENA

Diploma Thesis
by
Jürgen M.A. Winter

Physik-Department E15
Technische Universität München
September 2007

Abstract

The LENA (**L**ow **E**nergy **N**eutrino **A**stronomy) project comprises a 50 kt organic liquid-scintillator detector that is in the current design planned to be of cylindrical shape with a length of ∼100 m and a diameter of ∼30 m. The scintillation light is supposed to be detected with ∼13,000 photomultipliers (PMTs) installed at the inner wall. In order to shield the detector against cosmic rays and especially muons induced by these in the atmosphere, it will be necessary to place it either in an underground laboratory or on an abyssal plain. The goals of LENA are multidisciplinary, extending to the fields of astrophysics (e.g. the observation of supernova and solar neutrinos), particle physics (most importantly the search for proton decay), and geophysics.

The main part of this work is dedicated to the possible observation of neutrinos emitted by a galactic core-collapse supernova (SN) in the LENA detector. About $(1-2) \cdot 10^4$ events, depending on the SN model and neutrino oscillations, could be observed in real-time for an 8 $M_\odot$ SN in the centre of the our galaxy. Neutrino spectroscopy and high-statistics measurements of the total ν-flux and fluxes of the individual ν flavours would allow implications on the SN explosion mechanism and neutrino oscillation parameters.

Furthermore, the potential of spatial event reconstruction has been investigated. It is a tool that allows to tag delayed coincidence signatures and helps to define a fiducial volume in order to reduce external background. In this context, a Monte Carlo code was developed simulating the detector response to an event in the liquid scintillator. A maximum likelihood analysis applied to the hit pattern of the PMTs showed that a spatial resolution of ∼20 cm (1σ) can be achieved for a localised energy deposition of 10 MeV in the centre of the detector.

The spatial as well as the energy resolution are highly sensitive on the light yield of the scintillator. In the frame of this work, the light yield of two alternative scintillator components, namely LAB and PMP, was tested in an experimental setup. Comparison measurements to the default mixture of PXE, PPO and bisMSB show an equally good performance of the solvent LAB.

II

Contents

List of Figures

List of Tables

Chapter 1

Introduction

Ever since the first measurement of the solar neutrino flux deficit by the famous Homestake experiment of R. Davis in the early 1970s [1], the focus in neutrino physics was directed towards the determination of neutrino oscillation parameters rather than towards the monitoring of neutrino sources. Now, more than 30 years later, neutrino oscillations have been investigated and proven in a variety of experiments at different energy scales and a clear picture of the neutrino oscillations has been established. Apart from the mixing angle θ_{13}, the mass hierarchy and possible CP violating phases, the oscillation parameters are known with fairly high accuracy. Hence, a powerful tool is given for the comprehension of neutrino spectra and fluxes that are distorted by oscillations before reaching the detector. As a result, implications on the physical processes in the sources themselves are possible to a high level of precision.

Neutrinos are, as only weakly-interacting neutral particles, perfectly suited as probes for many processes where other types of particles are not able to deliver information. Unlike photons, they are hardly affected by matter densities. Unlike charged particles their propagation is not disturbed by electromagnetic fields. Hence, neutrinos still carry information on their creation processes when reaching Earth and pinpoint directly to their source. In the following, a variety of cosmic, natural and artificial sources of neutrinos shall be presented whose observation has already helped and might still in the future help to unravel mysteries in the fields of astroparticle-, particle- and geophysics, neutrino astronomy and cosmology.

A cosmic source of neutrinos are core-collapse supernovae (SN). In such explosions, a huge amount of energy is released in neutrinos of all flavours. Due to their enormous ν luminosity, SN can even be seen at large distances,

like the neutrinos from SN1987A in the Large Magellanic Cloud observed by the Kamiokande [2, 3] and the IMB [4, 5] detectors.

The measurement of solar neutrinos has been and still is a very productive and one of the most advanced areas in neutrino physics. As mentioned, the chlorine experiment of R. Davis in the Homestake mine [1] was the first experiment to give a hint on neutrino oscillations, measuring only about one third of the expected electron neutrino flux from the Sun. The SNO experiment [6] finally gave proof for solar neutrino oscillation, measuring with NC reactions the total flux predicted by the solar standard model while confirming the result from Davis on the ν_e-flux. Gallium based experiments like GNO [7], GALLEX [8] and SAGE [9] measuring the integrated flux with a low threshold and the water Čerenkov detector Super-Kamiokande [10], spectroscopically investigating the high-energy tail, supported this observation.

Only recently, Borexino [11] was the first experiment to do spectroscopy on low-energy solar neutrinos measuring ^{7}Be neutrinos. This constitutes another milestone in the comprehension of physical processes in the Sun and might also deliver information on solar neutrino oscillations.

A theoretical prediction has been made for the low-energy Diffuse Supernova Neutrinos (DSN), originating from core-collapse SNe happening throughout the history of the Universe. The best limit on DSN $\overline{\nu}_e$-flux has been determined by the Super-Kamiokande detector [12, 13]. A large-scale detector with a lower energy threshold and with a sufficient background reduction could be able to reach the necessary sensitivity for a first-time DSN observation.

Čerenkov detectors like BAIKAL [14] and AMANDA [15] observe the southern respectively northern hemisphere for high-energetic neutrinos, $\mathcal{O}$(GeV-TeV). So far, no cosmic point sources such as Gamma Ray Bursts (GRBs) or Active Galactic Nuclei (AGNs) could be identified, yet the sensitivity of the detectors is increasing steadily. Another possible ν source might originate from the annihilation of WIMPS (Weakly Interacting Massive Particles) that are assumed to make up Dark Matter. Due to their concentration in the centre of massive objects - like our galaxy, the Sun or even the Earth - they might be detected as point sources.

Atmospheric neutrinos are produced in the atmosphere in the decay of muon and pions that are created in collisions of cosmic rays (99% protons) with molecules in the upper atmosphere. The observation of oscillations

$\nu_\mu \to \nu_\tau$ of atmospheric neutrinos by the Super-Kamiokande detector [16] was a breakthrough in the establishment of the neutrino oscillation model.

Geoneutrinos, originating from natural radioactive elements (mainly Uranium, Thorium and their decay products, and ^{40}Ka) inside the Earth, have first been detected by the liquid-scintillator detector KamLAND [17]. A determination of their flux could be a key for a closer comprehension of the interior of our planet and its geological history.

Oscillations of reactor neutrinos, that means neutrinos that are produced by nuclear power plants, have been studied by various disappearance experiments and were finally observed by the KamLAND [18] detector. It confirmed the result from SNO on solar neutrino oscillation, determining the so-called large mixing angle solution for θ_{12}. The CHOOZ [19] reactor experiment holds the best limit on θ_{13}.

Another artificial source are neutrino beams that are produced in accelerator laboratories via the decay of pions. K2K [20] and MINOS [21] confirmed with their observation of $\nu_\mu \to \nu_\tau$ oscillations the results of Super-Kamiokande for atmospheric neutrino oscillations. The evidence for a sterile neutrino claimed by the LSND collaboration [22] has recently been refuted by the MiniBooNE experiment [23].

As illustrated, there is a huge variety of neutrino detectors investigating both neutrino oscillation parameters and neutrino sources. However, the urge to obtain more precise information motivates a new generation of detectors of a larger target masses in order to gain higher statistics. A selection of low-energy neutrino observatories under discussion is given in the following.

The planned megaton water Čerenkov detectors Hyper-Kamiokande [24] in Japan, MEMPHYS [25] in Europe and UNO [26] in the USA intend to to follow in the footsteps of the successful Super-Kamiokande detector. Due to their huge masses, they could provide very high statistics.

Another proposal for a large-scale detector is GLACIER [27, 28], a liquid Argon time projection chamber. This rather recently developed technique provides a very good particle identification.

Borexino and KamLAND have shown the huge potential of organic liquid-scintillator detectors, especially on the field of low-energy real-time neutrino spectroscopy. This states a big motivation for the design of larger liquid

scintillator detectors that allow high statistics observations like SNO+ [29], HanoHano [30] or the LENA detector [31, 32], a project that is introduced within this thesis.

LENA (Low Energy Neutrino Astronomy) is a 50 kt liquid-scintillator detector that is designed for a wide range of applications. Its low threshold of a few 100 keV, high energy resolution and fast timing would allow real-time spectroscopy of low-energy neutrinos (like solar or geoneutrinos [33]), while the large number of protons in the organic liquid scintillator makes the search for proton decay feasible [34]. Good background rejection enables as well the observation of DSN [35].

The three European large-scale detectors GLACIER, MEMPHYS and LENA are united in the LAGUNA (Large Apparatus for Grand Unification and Neutrino Astrophysics) collaboration in order to face common tasks. Results of the attainable performances of the three projects in the fields of proton decay, astro- and geoneutrino detection, and for future neutrino beams are presented in [36], along with a discussion about possible underground laboratories.

The variety of capabilities of the LENA (Low Energy Neutrino Astronomy) detector is reflected in the wide range of topics covered in this thesis. In the second Chapter, the LENA project will be discussed in more detail. Its physics potential is presented along with a possible detector design and the requirements for the liquid scintillator.

The possible detection of supernova neutrinos in LENA makes up a major part of this thesis. Therefore, an introduction to the current picture of the SN explosion mechanism is given in the third Chapter. Neutrino oscillations are presented in Chapter 4 as they largely affect the SN-ν event rates that are calculated for the LENA detector in Chapter 5.

The experimental work that was performed in the course of this thesis is introduced in the sixth Chapter, where the light yield measurement of some possible liquid scintillators for the LENA detector is presented. The scintillation light yield is a property of liquid scintillators that affects to a large extent the spatial and the energy resolution of the detector.

The seventh Chapter is dedicated to spatial event reconstruction of events in the LENA detector. This is important for the identification of delayed coincidence signals, e.g. occurring in detection reactions of SN-ν, and external background rejection.

Chapter 2

The LENA project

The LENA (Low Energy Neutrino Astronomy) detector is a 50 kt liquid-scintillator multipurpose detector which is currently in its planning stage.
In this Chapter, its physics capabilities are discussed. Furthermore, the detector design and possible locations are briefly presented along with a model on the functioning of liquid scintillators.

2.1 Physics Capabilities

The LENA detector could offer many possibilities to answer a variety of physics questions, thanks to a low energy threshold, high energy resolution, and a large detector volume. A brief overview of its potential including astrophysics, geophysics, and particle physics is presented in this section.

2.1.1 Supernova Neutrinos

Core-collapse supernovae (SN), classified as type-Ib, -Ic, and -II supernovae, happen in our galaxy roughly 1-3 times a century [37, 38]. Neutrinos and antineutrinos of all flavours are produced in such an event. LENA has several reaction channels for the detection of SN-ν, allowing both neutrino spectroscopy and the determination of the total ν flux. For a SN at the centre of our galaxy (~ 10 kpc) and an initial mass of 8 M$_\odot$ a fluence of $\sim 1.5 \cdot 10^{12}$cm^{-2} is expected. About 10,000 to 15,000 events - depending on the supernova model which the calculations are based on - offer the possibility to investigate both supernova physics and neutrino properties.
As the calculation of SN neutrino event rates in LENA constitutes a main part of this thesis, SN physics will be discussed more thoroughly in Chapter 3.

2.1.2   Diffuse Supernova Neutrinos

Under the assumption that core-collapse supernovae took place throughout the history of our universe, an isotropic neutrino background should be existent, the so-called Diffuse Supernova Neutrinos (DSN). Their detection would allow to learn more about the temporal evolution of the supernova rate as well as about different supernova models.

In LENA, $\overline{\nu}_e$ from the DSN can be detected most easily, via the inverse β-decay $\overline{\nu}_e + p \rightarrow n + e^+$. Mainly low energy atmospheric and reactor $\overline{\nu}_e$ contribute to the background. However, there is an almost background-free energy window between about 10 MeV and 25 MeV, depending on the geographical location of the detector itself (Figure 2.1). The best experimental limit on the DSN flux provided by the Super-Kamiokande experiment [12, 13] is 1.2 cm^{-2}s^{-1} for $E_{\overline{\nu}_e} > 19.3$ MeV (90% C.L.). Considering a flux of 1.5 cm^{-2}s^{-1}MeV^{-1} at 10 MeV [39] one expects 10 events per year in LENA [35]. After ~ 10 years of observation a spectral analysis of the DSNB is possible, allowing implications on core-collapse supernova models and SN rate up to redshifts z $\simeq 2$. If no signal was detected during that time, a new limit on the DSN flux could be set to 0.13 cm^{-2}s^{-1} for $E_{\overline{\nu}_e} > 19.3$ MeV.

2.1.3   Solar Neutrinos

Solar neutrinos are a fundamental key in understanding our Sun, as they represent a probe for solar fusion processes. Therefore, various experiments have been conducted or are still taking data in this field of research. Super-Kamiokande [10] and SNO [6] have measured the solar spectrum above a threshold of 5.5 MeV. Gallium based experiments like GALLEX [8], GNO [7], and SAGE [9] have only been sensitive to the integrated spectrum, yet with a much lower threshold. Recently, the liquid-scintillator detector Borexino first measured the ^{7}Be-ν solar neutrino rate in real-time [11].

In LENA, rates of ~ 5400 d^{-1} for ^{7}Be-ν, ~ 150 d^{-1} for pep-ν, and ~ 210 d^{-1} for CNO-ν are expected. For ^{8}B $- \nu$ event rates of $\sim 20,000$ a^{-1} and ~ 360 a^{-1} are estimated for the elastic scattering off electrons and ^{13}C, respectively. Using these measurements, the well-known solar luminosity, and ν-oscillation parameters, the pp-flux could be determined to an accuracy better than 0.5%. Due to the extremely high statistics on ^{7}Be-ν, LENA could be able to look for changes in the ^{7}Be $- \nu$ flux caused by temporal fluctuations of the solar density profile. Spectroscopy on pep-ν could be used to investigate the MSW effect in the transition region between 1-2 MeV. A day-night asymmetry of about 1% of the ^7Be-ν flux induced by the Earth Matter Effect [43, 44, 45] might come within reach, too.
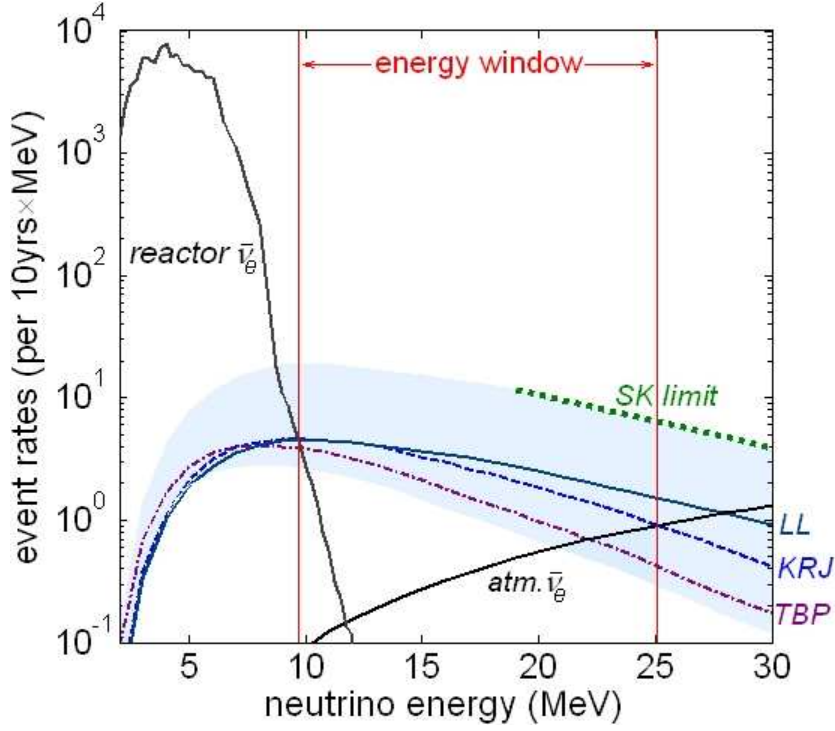
Figure 2.1: Expected DSN spectrum in LENA for different SN models (Lawrence Livermore group (LL) [40], Keil, Raffelt, and Janka (KRJ) [41], and Thompson, Burrows, and Pinto (TBP) [42]) as well as the Super-Kamiokande limit [13]. Reactor and atmospheric $\overline{\nu}_e$ rates (for the detector location in Pyhäsalmi (Finland)) contributing to the background in LENA are shown in black. The blue band shows the uncertainty of the DSN rates in LENA due to the imprecisely known SN rate. As depicted, an energy window between approximately 10 MeV and 25 MeV would allow the detection of DSN. From [35].

2.1.4 Terrestrial Neutrinos

Terrestrial neutrinos, also called geoneutrinos, are produced in the decay chains of Uranium and Thorium and the decay of ^{40}Ka embedded in the Earth's core, mantle and crust. These radioactive decays contribute to more than half of the Earth's thermal heat flow of about 60 mW m^{-2}, yet quantitative information is wanted for a better comprehension of the interior of the Earth. Recently, terrestrial neutrinos have been detected for the first time by the KamLAND detector [17].
LENA would detect terrestrial neutrinos via $\overline{\nu}_e + p \rightarrow n + e^+$ with a threshold of 1.8 MeV, and therefore only be sensitive to $\overline{\nu}_e$ from U and Th decay chains. The choice of the detector location is crucial for the measurement as reactor neutrinos state a large background. In LENA an event rate between ~ 500 a^{-1} and ~ 1000 a^{-1} is estimated for a detector location at Hawaii or Pyhäsalmi (FIN), respectively [33].

2.1.5 Proton Decay

Grand Unified Theories are among the most appealing candidates for physics beyond the standard model. One prediction of these theories is the decay of the proton. The current limit on the partial lifetimes of the proton has been set by the Super-Kamiokande experiment to $\tau_p > 2.3 \cdot 10^{33}$ a (at 90% C.L.) for the decay channel $p \rightarrow K^+ + \overline{\nu}$ [46] and $\tau_p > 5.4 \cdot 10^{33}$ a (at 90% C.L.) for $p \rightarrow e^+ + \pi^0$ [47].
The large number of both free and bound protons enables the search for proton decay in LENA. Many supersymmetric theories favour the decay mode $p \rightarrow K^+ + \overline{\nu}$, where a clear signature in LENA can be identified due to the delayed coincidence signal of the Kaon and the particles from its decay. In LENA, after 10 years of detection without a proton decay observation, the sensitivity could be pushed forward to $\tau_p > 4 \cdot 10^{34}$ a [34]. This value is already in the region of many theoretical predictions [48]. In the energy region of interest, mainly atmospheric neutrinos are a background for the detection of the proton decay.

2.1.6 Atmospheric Neutrinos

Collisions of cosmic rays (99% protons) with nuclei in the Earth's upper atmosphere lead to a production of $\mu^\pm$ and $\pi^\pm$. Subsequently, ν_e, $\overline{\nu}_e$, ν_μ, and $\overline{\nu}_\mu$ are produced in their decay. Neglecting neutrino oscillations, the ratio ν_e/ν_μ should be close to 1/2. It has been the Super-Kamiokande [16] detector first measuring a deviation in the expected zenith-angle dependance in the ν_e/ν_μ

ratio, thus giving proof for the oscillations between ν_μ and ν_τ.

In LENA, detailed information about atmospheric neutrinos could be obtained in the low energy part of the spectrum ($\sim$ 0.1-1 GeV). The quasi-elastic reactions $\overline{\nu}_e + p \rightarrow n + e^+$ and $\overline{\nu}_\mu + p \rightarrow n + \mu^+$ might be distinguishable, as the muon decays via $\mu^+ \rightarrow e^+ + \nu_e + \overline{\nu}_\mu$ with a high probability within the detector, resulting in a delayed coincidence signature. This could lead to high statistics measurements of oscillation parameters for low energy atmospheric neutrinos.

2.1.7 Long Baseline Experiments

The LENA detector could also be used for the detection of a neutrino beam coming from artificial sources such as new particle accelerators [49]. In such an oscillation experiment, topics of interest are the mixing angle θ_{13}, CP-violation in the leptonic sector, and matter effects. Studies on beta beams [36] showed, that electron-like and muon-like events can be separated on account of the delayed decay of the muon for low energies (0.2-1.2 GeV) and pulse shape analysis for higher energies. Both would work best if the beam was directed along the detector axis.

2.2 The LENA Detector

2.2.1 Detector Design

The LENA detector is planned to be of cylindrical shape with a length of about 100 m and a diameter of 30 m. The shape, namely the radius of the cylinder, is directly correlated to the attenuation and scattering length of the liquid scintillator that are in the order of 10 m [50]. In current studies, the inner vessel is intended to have a length 96 m and a radius of 13 m and will be filled with $\sim$ 50 kt of liquid scintillator (Figures 2.2, 2.3). It is planned to be surrounded by a 2 m wide, water filled muon veto. Depending on the specific measurement and the radiopurity of the liquid scintillator, the fiducial volume of the detector will lie within the inner vessel with a radius of max. 12 m.

The inner vessel will be equipped with about 13,000 photomultiplier tubes (PMTs) in order to collect scintillation light. At present, studies consider 50 cm diameter PMTs, while it would also be possible to equip smaller PMTs with light concentrators in order to reach a surface coverage of about 30%. PMTs in the muon veto serve for the detection of Cherenkov light of passing muons.
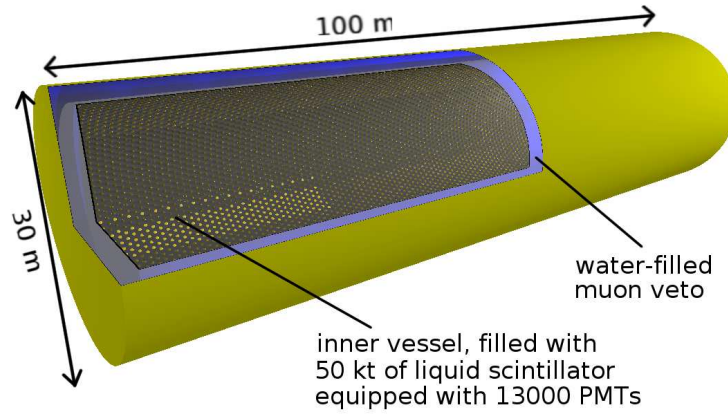
Figure 2.2: The LENA detector in its current design with a length of 100 m and a diameter of 30 m. The inner vessel is planned to have a diameter of 13 m, to contain 50 kt of liquid scintillator, and to be equipped with $\sim$ 13,000 PMTs. In current studies, it is surrounded by a 2 m thick water-filled muon veto.
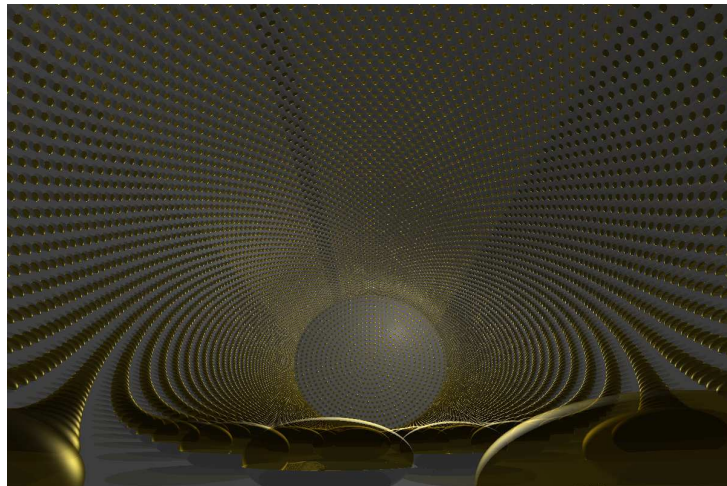

Figure 2.3: Artistic inner view of LENA.

2.2.2 Detector Location

Shielding from cosmic rays and muons is the most important criterion for the selection of suitable detector locations. Eventually, one can either choose an underground laboratory or an underwater abyssal plain. A shielding of at least 4000 m.w.e. (metres water equivalent) is desirable for LENA, i.e. for the detection of solar neutrinos and the observation of inverse β-decay where cosmogenic neutrons are background. Furthermore, the distance to nuclear plants is crucial as reactor $\overline{\nu}_e$ form a low energy background, especially for DSN and terrestrial neutrino detection. The latter is sensitive on the geographical position as well, since the terrestrial neutrinos flux differs for oceanic or continental crust. If Lena was used as a detector for a long baseline experiment, the distance to a corresponding accelerator laboratory would have to be taken into account.

Currently, there are several locations under discussion. In Europe, there are the underground laboratories in Boulby (UK), Canfranc (Spain), Fréjus (France), Pyhäsalmi (Finland), and Sieroczewice (Poland) and the underwater site offshore of Pylos (Greece). Potential American sites are Henderson mine (Colorado), Homestake mine (South Dakota), Kimballton mine (Virginia) and offshore near Hawaii. Table 2.1 shows a comparison of all locations concerning shielding and reactor neutrino flux.

Site	Shielding [m.w.e.]	Reactor $\overline{\nu}_e$ flux [cm^{-1}s^{-1}]
Boulby	2800	-
Canfranc	2450	-
Fréjus	4800	$1.6 \cdot 10^6$
Pyhäsalmi	4060	$1.9 \cdot 10^5$
Pylos	4000	$1.1 \cdot 10^5$
Sieroczewice	2200	-
Hawaii	≥ 4000	$1.1 \cdot 10^4$
Henderson	3100 (4200*)	$7.4 \cdot 10^4$
Homestake	4200	$7.5 \cdot 10^4$
Kimballton	1450 (4500*)	$6.4 \cdot 10^5$

Table 2.1: Comparison of potential LENA locations regarding shielding and reactor $\overline{\nu}_e$ flux (*= planned excavation).

2.3   Liquid Scintillator

The organic liquid scintillator is a mayor concern in the development of the
LENA detector, as it acts as target and detector at the same time. Its prop-
erties determine to a large extent the quality of the experiment. In the focus
of the research are characteristics such as light yield (see Chapter 6), flu-
orescence decay time, attenuation length, chemical long term stability and
radiopurity. Safety aspects like toxicity and flash point are regarded as well.
An organic liquid scintillator is usually a mixture of a solvent with one or
more fluors (also called wavelength shifter) that are added in concentration of
a few g/ℓ. Main components of the solvent are hydrogen and carbon, which
effectively serve as target for the incident particles. The solvent serves as
target and as source of scintillation light, whereas the fluor shifts the wave-
length to a level where the solvent is transparent for the light. An attenuation
length in the order of the radius of the detector is required in order to guar-
antee that photons emitted in the center of the detector efficiently reach the
photomultipliers. Due to a high light yield of 10^2 pe[1]/MeV and a sufficient
surface coverage, the number and time distribution of the detected photons
can be used to gain information about the energy of the incident particle.
Solvents under current investigation are Phenyl-o-Xylylethane (PXE) and
different purified types of Linear Alkylbenzene (LAB).

Fluors under investigation are 2,5-Diphenyloxazole (PPO), para-Terphenyl
(pTP), 1-Phenyl-3-Mesityl-2-Pyrazolin (PMP), and 1,4-bis-(o-methylstyryl)-
benzole (bisMSB). Some linear hydrocarbons (e.g. dodecane or tetradecane)
might also be added in order to increase the ratio of free protons to carbon.
This would be helpful for the detection of $\overline{\nu}_e$.

---

[1]photo electrons

Chapter 3

Supernova Physics

The observation of neutrinos of SN1987A in the Kamiokande detector [2, 3] and the IMB detector [4, 5] has been a milestone in the comprehension of core collapse supernovae. However, since only 11 and 8 events have been recorded in Kamiokande and IMB, respectively, it is difficult to make tight constraints on supernova models. As will be shown in Chapter 5, LENA could provide high statistics measurements for a galactic supernova (SN) and thus lead to a deeper understanding of SN physics.

In this Chapter, an introduction to SN physics is given. The current picture of the SN explosion mechanism will be explained as a whole in order to ensure a better comprehension of this complex process. Neutrino production mechanisms are especially pointed out in this context. This Chapter, along with the following Chapter 4 about neutrino oscillations in matter provides a basis for Chapter 5, where the event rate calculations of SN neutrino events in LENA are performed.

As mentioned in Chapter 2, a "standard supernova scenario" is assumed throughout this thesis: a progenitor star at a distance of 10 kpc (corresponding to the distance of the Earth to the center of the Milky Way) with about $8\,\mathrm{M}_\odot$ releasing $3 \cdot 10^{53}\mathrm{erg}$[1] of gravitational energy during the explosion.

3.1 Core-Collapse SN theory

Towards the end of their life, stars with masses $> 8\,\mathrm{M}_\odot$ build up a shell structure with an iron core in the centre [51]. Initially, the pressure of the degenerate electron gas in the iron core compensates the gravitational pull of the core itself. As more and more iron is produced in stellar fusion, the core's density continuously increases. At $\rho_{core} \approx 10^9$ g cm^{-3}, electron capture on

---

[1]1 erg = 10^{-7} J = $6.24 \cdot 10^5$ MeV

iron,

$$e^- + {}^{56}Fe \rightarrow {}^{56}Mn + \nu_e$$
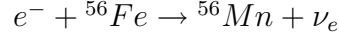
leads to a reduction of the electron pressure and thus induces the collapse of the core. Moreover, endothermic photodissociation of iron nuclei occurring for $T > 5 \cdot 10^9$ K),

$$\gamma + {}^{56}Fe \rightarrow 13\alpha + 4n - 124.4 \text{ MeV},$$
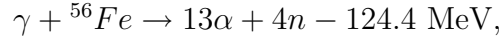
reduces the thermal pressure support, additionally exhausting the internal energy produced by the contraction, and thus enhances the collapse further. The star's outer layers are at first not affected by the collapse.

At densities of $\rho_{core} \approx 10^{11}$ g cm^{-3}, the neutrino mean free path gets in the order of the size of the iron core. As a result, neutrinos cannot escape freely from the core but rather propagate diffusely, whereas coherent scattering on nuclei dominates. This is called "neutrino trapping". As density decreases with radius, one can define a "neutrinosphere" in analogy to the photosphere of the Sun, an effective spherical surface radiating neutrinos. Outside the surface, neutrinos are able to stream freely. The radius of the neutrinosphere is energy and flavour dependent, as neutrino opacities show these dependencies. Inside the neutrinosphere, the neutrinos are in a thermal equilibrium and therefore their spectra are thermal.

When the density of the iron core reaches about $\rho_{core} \approx 3 \cdot 10^{14}$ g cm^{-3}, repulsive nuclear forces halt the collapse and drive a shock wave into the outer core. This process is known as "core bounce". In the prompt explosion scenario, the shock wave propagates outwards undisturbed and blows the stellar envelope off, resulting in a visible explosion. However, SN simulations indicate that the shock wave passes the neutrinosphere but does not reach the outer layers. In fact, it stalls due to two processes: First, the dissociation of iron nuclei, costing 8.8 MeV per nucleon, and second, the electron capture

$$e^- + p \rightarrow n + \nu_e$$
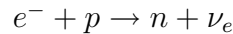
that takes place behind the shock.

The ν_e produced in the second process are trapped until the shock wave reaches the neutrinosphere, where suddenly a vast number of neutrinos can

escape freely in a short time. This is the so-called neutronisation burst which has a peak luminosity $> 10^{53}$erg s^{-1}. However, only 10^{51}erg (roughly 1% of the stars binding energy) are released in this burst because of its short duration of about 20 ms.

In the hot post-bounce region, $\overline{\nu}_e$ are produced via

$$e^+ + n \rightarrow p + \overline{\nu}_e, \qquad (3.1)$$

and ν_e via

$$e^- + p \rightarrow n + \nu_e. \qquad (3.2)$$

$\mu-$ and $\tau - \nu$ are produced by e^+e^- annihilation, nucleon-nucleon bremsstrahlung, and $\nu_e\overline{\nu}_e$ annihilation. These neutrinos carry 99% of the core's gravitational binding energy. As mentioned above, the size of the neutrinosphere depends on the opacities for the neutrinos. Due to charged-current interactions, the opacity for electron type neutrinos is higher than for μ- or τ-neutrinos. Moreover, since neutrons are more abundant than protons in the proto-neutronstar, the opacity for $\overline{\nu}_e$ (and therefore the radius of the $\overline{\nu}_e$-neutrinosphere) is smaller than for ν_e. The larger the size of the neutrinosphere is, the lower are the neutrino temperatures and thus their average energies. Hence, an observable hierarchy of the average neutrino energies is expected, inversely proportional to the opacities: $E_{\nu_x} > E_{\overline{\nu}_e} > E_{\nu_e}$, where ν_x stands for ν_μ, $\overline{\nu}_\mu$, ν_τ, and $\overline{\nu}_\tau$.

A probable solution for the revival of the stalled shock is the so-called neutrino heating mechanism, first proposed by Colgate and White [52]. With the help of this mechanism, Wilson [53] obtained a successful explosion in a simplified model.

If a sufficient amount of energy ($\mathcal{O}(10^{51}$ erg)) is transferred from the neutrinos produced in the nascent neutron star to the stalled shock, it can be revived leading to a successful explosion in which the stellar envelope blows off. The energy is transferred via the reactions

$$\nu_e + n \rightarrow p + e^-, \qquad (3.3)$$
$$\overline{\nu}_e + p \rightarrow n + e^+. \qquad (3.4)$$

Considering that $\sim 3 \cdot 10^{53}$erg gravitational binding energy are released in the explosion, only 1% needs to be transferred by the neutrinos. In the stellar

envelope, photodissociation is negligible and the shock waves can drive the successful explosion, which takes from several hours to days. This explosion mechanism is referred to as "delayed explosion".

The time scale of the cooling mechanism defines the duration of the thermal neutrino signal, which is about 10 to 20 seconds. One of the objectives of the LENA detector is to observe these neutrinos and thus help to learn more about the core collapse supernova explosion mechanism.

3.2   SN-ν spectra

As mentioned in the previous section, the core collapse SN-ν originate from 2 different processes: First, the ν_e from the neutronisation burst, second the thermal neutrinos produced in the hot and dense proto-neutron star. Flavour composition, luminosities and average energies differ for both cases.

The neutronisation burst lasts only for about 20 ms, while the peak luminosity reaches about 10^{53}erg s^{-1}. Electron neutrinos, produced in the reaction $p + e^- \rightarrow n + \nu_e$ behind the shock wave and being trapped at first, are suddenly able to escape freely when the shock reaches the neutrinosphere.

The thermal neutrinos are produced in the hot and dense proto-neutron star. ν_e and $\overline{\nu}_e$ are dominantly produced via 3.1 and 3.2 while the following reactions contribute to the production of all flavours:

- e^+e^--annihilation: $e^+e^- \rightarrow \nu\overline{\nu}$,

- nucleon-nucleon bremsstrahlung: $NN' \rightarrow NN'\nu\overline{\nu}$, and

- $\nu\overline{\nu}$-annihilation: $\nu\overline{\nu} \rightarrow \nu\overline{\nu}$.

All types of neutrino flavours are produced in these reactions.

Because of the high density in the core, the neutrinos cannot escape freely until they reach the neutrinosphere. Since they are in a thermal equilibrium, a Fermi-Dirac spectrum is expected. The time-integrated flux F_α^0 (the so-called fluence) as a function of the energy E is

$$F_\alpha^0(E) = \frac{L_\alpha}{NT_\alpha^3}\frac{E^2}{exp(E/T_\alpha) + 1}, \qquad (3.5)$$

where L_α is the number luminosity, T_α ($\alpha = \nu_e, \overline{\nu}_e, {}^{(}\overline{\nu}{}^{)}_x; x = \mu, \tau$) the effective neutrino temperature and N a normalisation factor. In fact, spectra obtained

in MC studies [40, 42] approximately show this dependency. This spectral form builds the basis for the calculation of the event rates for the SN simulations models of Lawrence-Livermore (LL) [40] and Thompson, Burrows, and Pinto (TBP) [42] performed in Chapter 5. Keil, Janka, and Raffelt (KRJ) [41] introduced a "pinched" Fermi-Dirac distribution. This way, they consider the finite width of the neutrinospheres due to the dependency of the interaction cross-sections on the neutrino energy. Therefore, neutrinos do not have perfect blackbody spectra:

$$F_\alpha^0(E) = \frac{L_\alpha}{NT^3} \frac{E^2}{exp(E/T_\alpha - \eta_\alpha) + 1}. \tag{3.6}$$

The pinching factor η_α usually is between 0 and 3. Figure 3.1 shows the difference of the pinched and unpinched spectra visually for the same average energy and normalised to 1. The pinched spectrum is found to be narrower and to have a suppressed high-energy tail with respect to the unpinched spectrum. This results in a lower event rate, since the relevant cross-sections in LENA scale proportional to the energy.
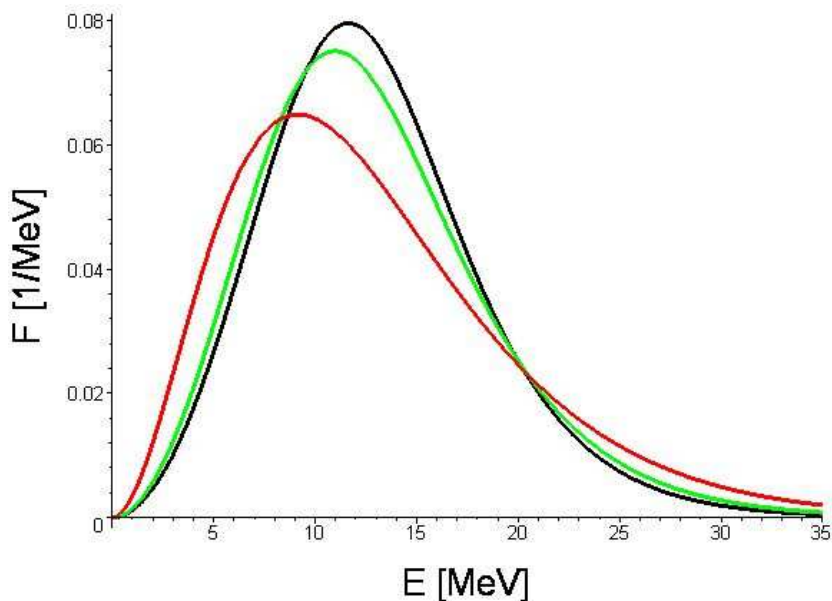

Figure 3.1: Normalised thermal spectra with different pinching factors; in red $\eta = 0$, in green $\eta = 2$, and in black $\eta = 4$. The pinched spectra have a suppressed high-energy tail with respect to the unpinched spectrum. Pinching occurs only in the SN model of Keil, Janka and Raffelt [41].

For the onset of the core collapse, the time evolution of the luminosities

and the average energy for each flavour can be seen in Figure 3.2 [54]. The ν_e luminosity rises fast, reaching a peak luminosity of about $3 \cdot 10^{53}$erg s^{-1}. This neutronisation burst lasts for about 20 ms. Later thermally produced ν_e dominate the ν_e luminosity. The luminosities of $\overline{\nu}_e$ and ν_x only show the characteristic of thermal neutrino production. The thermal spectra last for about 20s. Apart from the first 20 ms, the average energies show the predicted hierarchy $E_{\nu_x} > E_{\overline{\nu}_e} > E_{\nu_e}$ $(x = \mu, \tau)$.

3.3   SN-ν Detection Reactions in LENA

Overall, eight possible interaction detection reactions in liquid scintillator for SN neutrinos have been investigated. They are ordered into 4 charged current (CC) reactions for the detection of electron-type neutrinos and 4 neutral current (NC) reactions (including CC contributions for electron-type neutrinos). In this section, all 8 channels are briefly presented, mentioning their energy threshold. A closer discussion follows in Chapter 5.

Charged Current Reactions

channel no.	channel	E_{thr} [MeV]
1	$\overline{\nu}_e + p \rightarrow n + e^+$	1.8
2	$\overline{\nu}_e + {}^{12}\text{C} \rightarrow {}^{12}\text{B} + e^+$	14.39
3	$\overline{\nu}_e + {}^{12}\text{C} \rightarrow {}^{12}\text{B} + e^+$	17.34
4	$\nu_e + {}^{13}\text{C} \rightarrow {}^{13}\text{N} + e^-$	2.22

Neutral Current Reactions

channel no.	channel	E_{thr} [MeV]
5	$\nu_x + {}^{12}\text{C} \rightarrow {}^{12}\text{C}^* + \nu_x$	15.11
6	$\nu_x + p \rightarrow \nu_x + p$	-
7	$\nu_x + e^- \rightarrow \nu_x + e^-$	-
8	$\nu_x + {}^{13}\text{C} \rightarrow {}^{13}\text{C}^* + \nu_x$	3.68

The variety of channels for SN-ν in the LENA detector allows the independent measurement of different SN parameters. The total flux, that can be measured with the channels 5,7 and 8, and also the single fluxes can be determined. Information on the ν_e flux can be obtained with channels 1 and 2, on the $\overline{\nu}_e$ flux with 3 and 4. Since channel 6 is mostly sensitive to
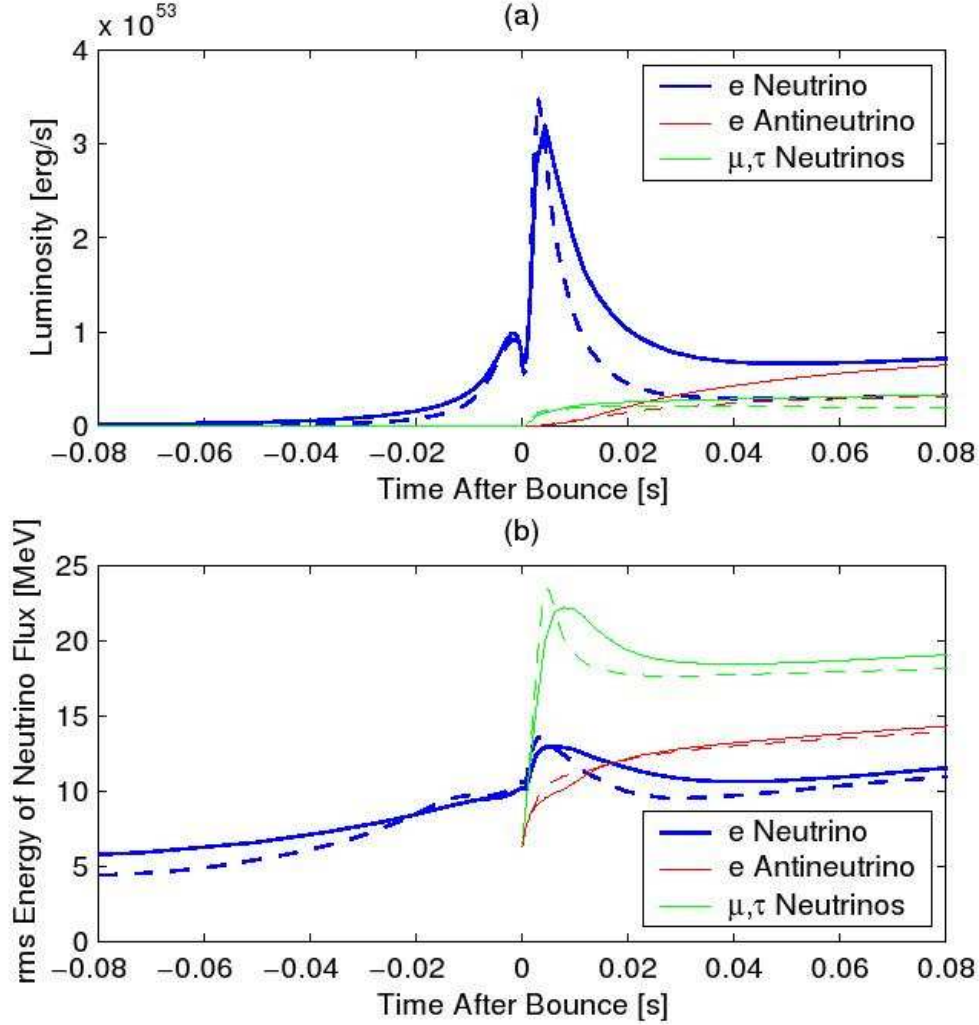
Figure 3.2: Time evolution of neutrino luminosities (a) and average energies (b). The solid and dashed lines represent calculations for progenitor masses of 40 $M_\odot$ and 13 $M_\odot$, respectively. The neutronisation burst of the ν_e dominates for the first 20 ms, while the luminosities from thermally produced neutrinos gain importance afterwards. As predicted, there is a hierarchy of average energies: $E_{\nu_x} > E_{\overline{\nu}_e} > E_{\nu_e}$ $(x = \mu, \tau)$. Taken from [54].

high energetic neutrinos, an estimation of the ν_x flux $(x = \mu, \tau)$ is possible. Spectroscopy is possible for all NC channels.

Chapter 4

Neutrino Oscillations

Neutrino oscillation is a phenomenon that is beyond the standard model of particle physics, since it violates lepton number conservation and requires massive neutrinos. Historically, the first hint has been delivered by the chlorine experiment of R. Davis [1], that measured about a third of the expected solar ν_e flux. This result however could have also been due to a wrong standard model of the Sun which the calculations were based on. Evidence for neutrino oscillation in the field of solar neutrinos has finally been given by the SNO [6] experiment, supported by measurements of GALLEX [8], GNO [7], and SAGE [9], and Super-Kamiokande [10]. In the field of reactor neutrinos, CHOOZ [19] and KamLAND [18] have made important discoveries for solar mixing parameters. Oscillation of atmospheric neutrinos has been proven by Super-Kamiokande [16]. Accelerator neutrino experiments like K2K [20] and MINOS [21] further investigated atmospheric mixing.

Neutrino oscillations have a strong impact on the SN neutrino spectra and hence SN event rate calculations done for the LENA detector will strongly depend on them (see Chapter 5). Therefore, an overview on neutrino oscillations in general is given in this chapter. As directly relevant for SN neutrinos, oscillations in matter and matter resonance are discussed thoroughly in the last section. This section follows the work of [55, 56].

4.1   Overview

Considering weak interaction, there are three kinds or flavours of neutrinos: ν_e, ν_μ, and ν_τ, also referred to as flavour eigenstates. In general, these flavour eigenstates do not coincide with the eigenstates of the free Hamiltonian, called mass eigenstates $|\nu_i\rangle$ (i=1,2,3), that possess a defined mass. The

transformation between these two bases is described by the Maki-Nakagawa-Sakata (MNS) matrix [56].

In general, a neutrino is produced in a weak interaction in a defined flavour eigenstate which can be expressed as a linear combination of the mass eigenstates according to the MNS matrix. In plane wave approximation, each mass eigenstate evolves as $\exp[\imath(E_i t - \overrightarrow{k}_i \cdot \overrightarrow{x})]$ (i = 1,2,3), where E_i and $\overrightarrow{k}_i$ denote energy and momentum of the mass eigenstate ν_i. As mass differences lead to different dispersion relations $E_i^2 = \overrightarrow{k}_i^2 + m_i^2$, phase differences between the mass eigenstate wave functions occur for propagating neutrinos (in time and space). The time evolved linear combination will usually be different from the original linear combination, what means that there will be a nonzero probability that the neutrino will be detected in a different flavour from the original. This effect is known as neutrino oscillation.

4.2 Neutrino Oscillations in Vacuum

The equation of motion for the neutrino mass eigenstates $|\nu_i\rangle$ (i = 1,2,3), neglecting spin degrees of freedom, under the assumption that all mass eigenstates have the same energy E and in a limit for ultra-relativistic neutrinos ($E_i = \sqrt{p^2 + m_i^2} \approx p + \frac{m_i^2}{2p} \approx E + \frac{m_i^2}{2p}$) is

$$\imath\nabla|\nu_i\rangle = -\left(E - \frac{M^2}{2E}\right)|\nu_i\rangle, \tag{4.1}$$

M stands for the mass matrix $M = \mathrm{diag}(m_1, m_2.m_3)$. For simplicity, $\hbar$ and c are set to 1.

The first term on the r.h.s. of Eq. (4.1) can be neglected, since it is proportional to the unity matrix, resulting in a common phase shift for all mass eigenstates. Thus, it does not contribute to neutrino oscillations and will not be considered further.

The mass eigenstates $|\nu_i\rangle$ describe stationary states that evolve in time according to the Schrödinger equation:

$$|\nu_i(t)\rangle = \exp(-\imath E t)|\nu_i\rangle. \tag{4.2}$$

As mentioned, the flavour eigenstates $|\nu_\alpha\rangle$ ($\alpha = e, \mu, \tau$) can be expressed

as a linear combination of the mass eigenstates $|\nu_i\rangle$ (i = 1,2,3) and vice versa:

$$|\nu_\alpha\rangle = \sum_i U_{\alpha i}|\nu_i\rangle, \tag{4.3}$$

$$|\nu_i\rangle = \sum_\alpha U_{\alpha i}^*|\nu_\alpha\rangle. \tag{4.4}$$

$U_{\alpha i}$ stand for the elements of the Maki-Nakagawa-Sakata matrix [56]. The unitary matrix can be parametrised in the following way, neglecting possible Majorana phases:

$$
\begin{aligned}
U &= \begin{pmatrix} 1 & 0 & 0 \\ 0 & c_{23} & s_{23} \\ 0 & -s_{23} & c_{23} \end{pmatrix} \begin{pmatrix} c_{13} & 0 & s_{13}e^{-i\delta} \\ 0 & 1 & 0 \\ -s_{13}e^{i\delta} & 0 & c_{13} \end{pmatrix} \begin{pmatrix} c_{12} & s_{12} & 0 \\ -s_{12} & c_{12} & 0 \\ 0 & 0 & 1 \end{pmatrix} \\
&= \begin{pmatrix} U_{e1} & U_{e2} & U_{e3} \\ U_{\mu 1} & U_{\mu 2} & U_{\mu 3} \\ U_{\tau 1} & U_{\tau 2} & U_{\tau 3} \end{pmatrix}.
\end{aligned} \tag{4.5}
$$

s_{ij} and c_{ij} (i=1,2,3) stand for $\sin(\theta_{ij})$ and $\cos(\theta_{ij})$, respectively, with the rotation mixing angles θ_{ij} and δ for a possible CP-violating phase.

The equations of motion, Eq. (4.1), can now be expressed in terms of the flavour eigenstates as

$$i\nabla|\nu_\alpha\rangle = \frac{UM^2U^\dagger}{2E}|\nu_\alpha\rangle,. \tag{4.6}$$

It should be noted, that the term $UM^2U^\dagger$ is in general not diagonal.

Now, consider a neutrino produced in weak interaction with an arbitrary flavour α. At the time t=0, it can be expressed in the system of the mass eigenstate basis as

$$|\nu_\alpha\rangle = |\nu(t=0)\rangle = \sum_i U_{\alpha i}|\nu_i\rangle. \tag{4.7}$$

Using 4.2 and 4.4, the wave function at time t can be written as

$$|\nu(t)\rangle = \sum_{i,\beta} U_{\alpha i}U_{\beta i}^* \exp(i\frac{m_i^2}{2E}t)|\nu_\beta\rangle. \tag{4.8}$$

The probability that an neutrino changes its flavour from α to β, can be calculated to

$$
\begin{aligned}
P_{\alpha\beta} &= |\langle \nu_\beta | \nu \rangle|^2 \\
&= \left| \sum_i U_{\alpha i} U_{\beta i}^* \ \exp(-\imath (E + \frac{m_i}{2E})t) \right|^2 \\
&= \sum_{i,j} U_{\alpha i} U_{\alpha j}^* U_{\beta i}^* U_{\beta j} \exp(-\imath \frac{\Delta m_{ij}^2}{2E} t).
\end{aligned}
\qquad (4.9)
$$

with $\Delta m_{ij}^2 = m_i^2 - m_j^2$, and is in general non-zero. Obviously, neutrino oscillations only occur for non degenerate masses.

In a simple case of 2 flavours (denoted ν_e and ν_μ here), one mass square difference Δm^2 mixing angle θ suffices to describe the system. Eq. (4.9) simplifies to

$$
P_{e\mu} = \sin^2 2\theta \sin^2 \left(\frac{\pi z}{l_{osc}} \right), \qquad (4.10)
$$

where

$$
l_{osc} = \frac{4\pi E}{\Delta m^2} = 2.48 \cdot 10^7 \text{ cm } \left(\frac{E}{1\text{MeV}} \right) \left(\frac{10^{-5}\text{eV}^2}{\Delta m^2} \right) \qquad (4.11)
$$

is called the oscillation length in vacuum.

The current best values for the mixing angles θ_{ij} and the mass square differences Δm_{ij}^2 are [57]

$$
\begin{aligned}
\Delta m_{21}^2 &= (8.0 \pm 0.3) \cdot 10^{-5}\text{eV}^2 & (4.12) \\
1.9 \cdot 10^{-3}\text{eV}^2 < |\Delta m_{32}^2| &< 3.0 \cdot 10^{-3} \text{ eV}^2 & (4.13) \\
\sin^2 2\theta_{12} &= 0.86^{+0.03}_{-0.04} & (4.14) \\
\sin^2 2\theta_{23} &> 0.92 & (4.15) \\
\sin^2 2\theta_{13} &< 0.19 & (4.16)
\end{aligned}
$$

Of θ_{13} only an upper bound is known. The unknown sign of Δm_{32}^2 leaves two possibilities of mass hierarchies of the neutrino mass eigenstates: the so-called normal ($m_3 > m_2 > m_1$) and inverted ($m_2 > m_1 > m_3$) hierarchy.

4.3   Neutrino Oscillations in Matter

If neutrinos propagate in matter instead of vacuum, their oscillation behaviour changes due to the interaction of electron neutrinos with the electrons present in matter. Neutrino oscillations in matter have firstly been

investigated by Wolfenstein [44]. If the matter density is constant, the situation is essentially like in the vacuum case, yet with different mixing angles. In case of a varying matter density a resonance effect can occur, which is able to enhance the transition probability maximally. This resonance has been discovered by Mikheyev and Smirnov [43], and is referred to as Mikheyev-Smirnov-Wolfenstein (MSW) effect. The MSW effect plays an important role for solar neutrinos and moreover, for SN neutrinos.

4.3.1 Constant Matter Density

The interaction with matter can be considered in the oscillation formalism with the introduction of an effective potential to the equation of motion

$$\imath\nabla|\nu_\alpha\rangle = \left(A + \frac{UM^2U^\dagger}{2E}\right)|\nu_\alpha\rangle. \tag{4.17}$$

A represents the contribution from interactions with matter.

$$A = \frac{G_F n_B}{\sqrt{2}} \begin{pmatrix} 3Y_e - 1 & 0 & 0 \\ 0 & Y_e - 1 & 0 \\ 0 & & Y_e - 1 \end{pmatrix} \tag{4.18}$$

G_F is the Fermi constant, n_B the baryon density, and Y_e the electron number fraction per baryon. Only contributions from the interaction with electrons enter into the additional potential A since the different neutrino flavours couple differently to electrons. While all flavours interact via neutral current, ν_e undergo also charged current interactions.

In a simple case of only 2 neutrino flavours, it is easier to understand the effect of matter on the oscillations. In a straightforward way, the equation of motion for mass eigenstates in matter can be written according to the 2 flavour case in vacuum:

$$\imath\nabla \begin{pmatrix} \nu_e \\ \nu_\mu \end{pmatrix} = \frac{\Delta m_m^2}{4E} \begin{pmatrix} -\cos2\theta_m & \sin2\theta_m \\ \sin2\theta_m & \cos2\theta_m \end{pmatrix} \begin{pmatrix} \nu_e \\ \nu_\mu \end{pmatrix}, \tag{4.19}$$

again neglecting terms proportional to the identity matrix. The angle θ_m is the mixing angle representing the matter case. The modified parameters for the matter case are related to the parameters in vacuum:

$$\sin 2\theta_m = \frac{\sin 2\theta}{\sqrt{(\xi - \cos 2\theta)^2 + \sin 2\theta}} \tag{4.20}$$

and

$$\Delta m_m^2 = \Delta m^2 \sqrt{(\xi - \cos 2\theta)^2 + \sin 2\theta}. \tag{4.21}$$

The dimensionless density parameter ξ is equal to

$$
\begin{aligned}
\xi &= \frac{2\sqrt{2}G_F n_B E}{\Delta m^2} \\
&= 1.53 \cdot 10^{-2}\left(\frac{Y_e \rho}{1\mathrm{g}\ \mathrm{cm}^{-3}}\right)\left(\frac{E}{1\mathrm{MeV}}\right)\left(\frac{10^{-5}\mathrm{eV}^2}{\Delta m^2}\right).
\end{aligned}
\tag{4.22}
$$

Analog to the oscillation length in vacuum (Eq. (4.11)), the oscillation length in matter is defined as

$$
l_{osc,m} \equiv \frac{4\pi E}{\Delta m_m^2} = \frac{\sin 2\theta_m}{\sin 2\theta}l_{osc}.
\tag{4.23}
$$

For $\xi = \cos 2\theta$, the mixing angle in matter θ_m gets maximal, $\frac{\pi}{4}$. This case of maximal flavour conversion is called resonance. The resonance density ρ_{res} can be derived from Eq. (4.22) and is

$$
\rho_{res} = 1.3 \cdot 10^2\ \mathrm{g}\ \mathrm{cm}^{-3}\cos 2\theta\left(\frac{0.5}{Y_e}\right)\left(\frac{1\mathrm{MeV}}{E}\right)\left(\frac{\Delta m^2}{10^{-5}\mathrm{eV}^2}\right).
\tag{4.24}
$$

At the resonance density, the mass square difference (4.21) is minimal, and the oscillation probability gets one.

4.3.2 Varying Matter Density

Starting with the equation of motion, according to 4.1.

$$
i\nabla U^\dagger|\nu_\alpha\rangle = \frac{M^2 U^\dagger}{2E}|\nu_\alpha\rangle.
\tag{4.25}
$$

Attention has to be paid to the rotation matrix U, where the mixing angle θ_m now depends on a varying density and thus is position dependent. Multiplying 4.25 with U and changing the basis yields

$$
i\nabla|\nu_{i,m}\rangle + iU(\nabla U^\dagger)|\nu_{i,m}\rangle = \frac{M^2}{2E}|\nu_{i,m}\rangle
\tag{4.26}
$$

Since ∇ and U do not commute, the equation cannot be diagonalised. Due to the dependency of θ_m on the position, the equation can in general not be solved analytically.

In order to get a clear picture of oscillation in varying matter density, the 2-flavour case will again be considered. The equation of motion for a wave

evolving in z direction is

$$\imath\frac{\partial}{\partial z}\left(\begin{array}{c}\nu_{1,m}\\\nu_{2,m}\end{array}\right)=\left(\begin{array}{cc}-\frac{\Delta m_m^2}{2\omega}&-\imath\frac{\partial\theta_m}{\partial z}\\\imath\frac{\partial\theta_m}{\partial z}&\frac{\Delta m_m^2}{2\omega}\end{array}\right)\left(\begin{array}{c}\nu_{1,m}\\\nu_{2,m}\end{array}\right)\tag{4.27}$$

Obviously, even the mass eigenstates mix for an inhomogeneous density.

If the matrix is approximately diagonal, meaning

$$\left|\frac{\partial\theta_m}{\partial z}\right|\ll\frac{\Delta m_m^2}{2\omega},\tag{4.28}$$

the mass eigenstates will not mix. Both ν_1 and ν_2 will stay the same as before. This is called "adiabatic" resonance. On the other hand, if condition (4.28) is not satisfied, mixing occurs, called "non-adiabatic" resonance. The mixing is maximal for large $\frac{\partial\theta_m}{\partial z}$, around the resonance point defined in Eq. (4.24). Naturally, the mixing of mass eigenstates also results in an observable oscillation of neutrino flavours.

An adiabaticity parameter γ can be derived from Eq. (4.28). It is defined as

$$\gamma\equiv\frac{\Delta m^2}{E\left|\frac{\partial ln(n_e)}{\partial z}\right|_{res}}\sin2\theta\,\tan2\theta.\tag{4.29}$$

Figure 4.1 shows the scenario for solar neutrinos. Comparing the solar density profile with 4.24, a mixing between $\nu_{1,m}$ and $\nu_{2,m}$ can occur in the Sun. In the interior of the Sun, ν_e coincides with $\nu_{1,m}$ because of the high densities. The adiabaticity of the resonance between $\nu_{1,m}$ and $\nu_{2,m}$ depends on θ_{12} and the neutrino energy. For example, in case of the adiabatic resonance $\nu_{1,m}$ changes to $\nu_{2,m}$ and can be detected on Earth as a ν_e with the probability $|U_{e2}|$. Hence, the original ν_e-flux predicted by the solar standard model is significantly lower. Due to the MSW effect, ν_e produced in the Sun are not necessarily detected as such in a detector on Earth. In the chlorine experiment of R. Davis [1], this ν_e flux deficit has been measured first. The SNO experiment [6] confirmed this result by the first observation of neutrino flavour transition. Moreover, the measured total flux was compatible with predictions from the solar standard model.

4.4   H/L-Resonance

The resonant conversions of neutrinos that can occur within a supernova are called H- and L- resonance (H for high, L for low density). Due to the
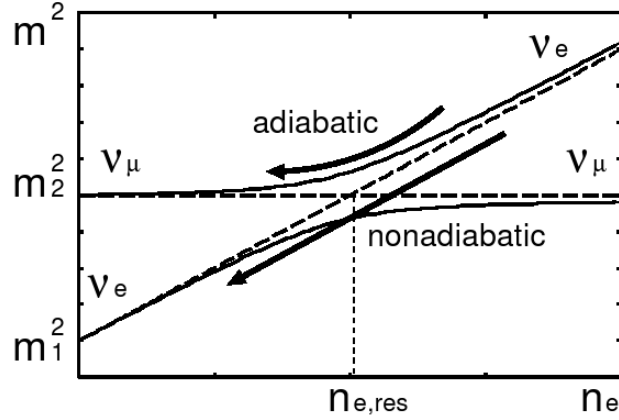
Figure 4.1: Effective mass squares as a function of the electron density n_e, increasing from right to left. As indicated by the arrows, $\nu_{i,m}$ stays $\nu_{i,m}$ for a non-adiabatic resonance and $\nu_{i,m} \rightarrow \nu_{j,m}$ for an adiabatic resonance. Due to this mass eigenstate mixing, neutrino fluxes of a defined flavour can change as well.

large mass gap $(\Delta m_{23}^2 \gg \Delta m_{12}^2)$ and the smallness of θ_{13}, the oscillations of the original 3-neutrino system can be described with the help of two 2-neutrino oscillations. The L-resonance is driven by $\Delta m_{12}^2 \approx 8 \cdot 10^{-5}$ eV^2 and θ_{12} and occurs for neutrinos only, while the H-resonance is driven by $\Delta m_{13}^2 \approx 2 \cdot 10^{-3}$ eV^2 and θ_{13} and occurs for neutrinos in the case of normal hierarchy $(m_3 > m_2 > m_1)$ and for anti-neutrinos in the case of inverted hierarchy $(m_2 > m_1 > m_3)$ (see Table 4.1).

	hierarchy	
	normal	inverted
ν-sector	H,L	L
$\overline{\nu}$-sector	-	H

Table 4.1: Occurrences of H- and L-resonance for ν_e and $\overline{\nu}_e$ for different scenarios.

According to Eq. (4.24) the L- and H-resonance occur at

$$\rho_L \approx (20 - 200) \text{ g cm}^{-3}, \rho_H \approx (1 - 10) \cdot 10^3 \text{ g cm}^{-3}. \qquad (4.30)$$

The resonance regions are far from the core, thus it is not expected that the

SN dynamics are affected by oscillation.

According to 4.29, the adiabaticity depends on the mixing angle involved. When putting the mixing angle involved in the L-resonance, $\sin^2 2\theta_{12} = 0.86$ [58], into 4.29, the result is that the L-resonance is perfectly adiabatic for typical SN-ν energies. For θ_{13} however, only an upper bound is known allowing still both an adiabatic or a non-adiabatic H-resonance dependent on the precise value of the mixing angle.

Figures 4.2 and 4.3 show schematically the resonances occurring for normal and inverted hierarchy, respectively. For normal hierarchy, both resonances occur in the neutrino sector whereas for inverted hierarchy the H-resonance occurs in the anti-neutrino sector and the L-resonance in the neutrino sector.

Following [59], the neutrino fluxes on Earth F_{ν_α} will be calculated depending on the original fluxes $F_{\nu_\alpha}^0$ ($\nu_\alpha = \nu_e, \overline{\nu}_e, \nu_x$). F_{ν_x} denotes the fluxes of $\nu_\mu, \overline{\nu}_\mu, \nu_\tau$, and $\overline{\nu}_\tau$ which are considered to be the same, since they interact almost in the same way with matter in the SN core.

For extremely high densities as in the SN core, the flavour eigenstates coincide with the mass eigenstates. In the case of normal hierarchy this means that $\nu_e = \nu_{3,m}$ and $\overline{\nu}_e = \overline{\nu}_{1,m}$. Due to the additional potential for CC-interaction the ν_e has the highest effective mass. The $\overline{\nu}_e$ has the lightest mass, since the potential enters negatively into Equation (4.17). Therefore, $\nu_e = \nu_{2,m}$ and $\overline{\nu}_e = \overline{\nu}_{3,m}$ for the inverted hierarchy.

A classification between ν_τ and ν_μ into mass eigenstates is not necessary since both fluxes are assumed to be the same, F_x.

Denoting the flip probabilities at the resonance points with P_H and P_L, the neutrino fluxes on Earth assuming normal hierarchy can be expressed as

$$F_i = a_i F_e^0 + (1 - a_i) F_x^0 \qquad (4.31)$$

where

$$
\begin{aligned}
a_1 &= P_L P_H, \\
a_2 &= (1 - P_L) P_H, \text{and} \\
a_3 &= 1 - P_H
\end{aligned}
\qquad (4.32)
$$

denote the contributions of the original ν_e flux, F_e^0, to F_i, the fluxes referring of the mass eigenstates in vacuum. Their coherence is lost on the way to
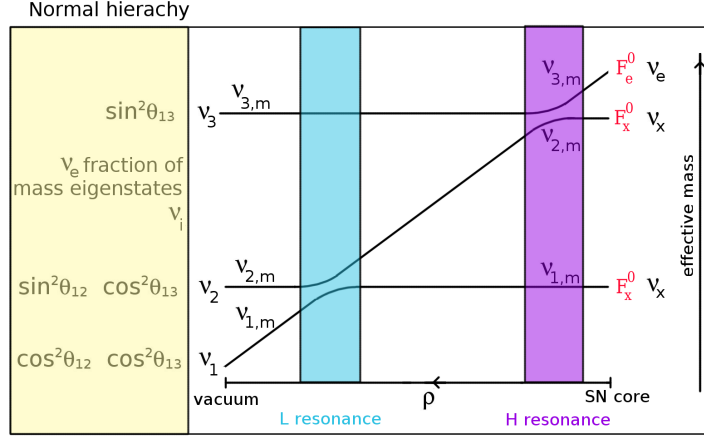
Figure 4.2: In case of normal hierarchy, both H- and L-resonance occur in the neutrino sector. The figure shows the evolution of the effective masses of the neutrino mass eigenstates with respect to the density. In the core, flavour and mass eigenstates coincide. A classification between ν_τ and ν_μ into $\nu_{1,m}$ or $\nu_{2,m}$ is not necessary since both fluxes are assumed to be the same, F_x. The H-resonance occurs between $\nu_{3,m}$ and $\nu_{2,m}$ for high densities ($\rho_H \approx (1-10) \cdot 10^3$ g cm^{-3}), whereas the adiabaticity depends on θ_{13}. The adiabatic L-resonance occurs for low densities ($\rho_L \approx (20 - 200)$ g cm^{-3}) between $\nu_{2,m}$ and $\nu_{1,m}$.

The left panel shows the electron neutrino fraction of the mass eigenstates in vacuum: $|U_{e1}|^2 = \cos^2\theta_{12} \cos^2\theta_{13}$, $|U_{e2}|^2 = \sin^2\theta_{12} \cos^2\theta_{13}$, and $|U_{e3}|^2 = \sin^2\theta_{13}$.

the Earth, so that the neutrinos arrive there as incoherent fluxes of the mass eigenstates.

Subsequently follows from neutrino mixing

$$
\begin{aligned}
F_{\nu_e} &= \sum_i |U_{ei}|^2 F_i \\
&= P_{ee} F_{\nu_e}^0 + (1 - P_{ee}) F_{\nu_x}^0,
\end{aligned}
\tag{4.33}
$$

where

$$
P_{ee} \equiv |U_{e1}|^2 P_L P_H + |U_{e2}|^2 (1 - P_L) P_H + |U_{e3}|^2 (1 - P_H)
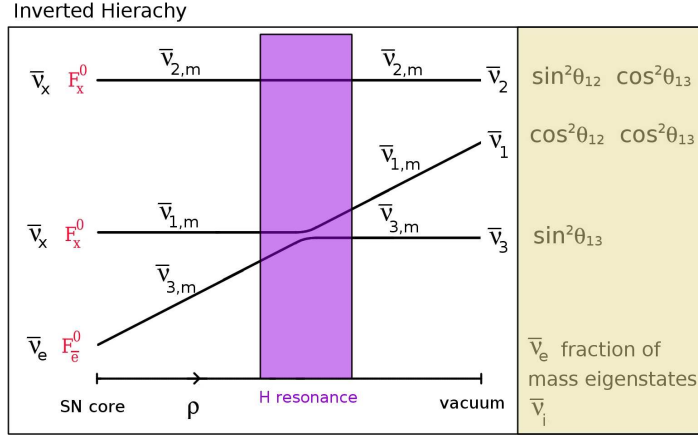\tag{4.34}
$$

Figure 4.3: In case of inverted hierarchy, the H-resonance occurs in the anti-neutrino sector. The figure shows the evolution of the effective masses of the neutrino mass eigenstates with respect to the density. In the core, flavour and mass eigenstates coincide. A classification between $\overline{\nu}_\tau$ and $\overline{\nu}_\mu$ into $\overline{\nu}_{1,m}$ or $\overline{\nu}_{2,m}$ is not necessary since both fluxes are assumed to be the same, F_x. The H-resonance occurs between $\overline{\nu}_{3,m}$ and $\overline{\nu}_{1,m}$ for high densities ($\rho_H \approx (1 - 10) \cdot 10^3$ g cm^{-3}), whereas the adiabaticity depends on θ_{13}. Not shown is the adiabatic L-resonance, occurring for low densities ($\rho_L \approx (20 - 200)$ g cm^{-3}) between $\nu_{2,m}$ and $\nu_{1,m}$ in the neutrino sector (see Figure 4.2).
The right panel shows the electron anti-neutrino fraction of the mass eigenstates in vacuum: $|U_{e1}|^2 = \cos^2\theta_{12} \cos^2\theta_{13}$, $|U_{e2}|^2 = \sin^2\theta_{12} \cos^2\theta_{13}$, and $|U_{e3}|^2 = \sin^2\theta_{13}$.

is the probability, that an electron neutrino produced in the SN is detected as such on Earth.

Due to flux conservation,

$$F_{\nu_\mu} + F_{\nu_\tau} = 2F_{\nu_x} = (1 - p)F_{\nu_e}^0 + (1 + p)F_{\nu_x}^0. \qquad (4.35)$$

Analogously, the fluxes can be calculated for inverted hierarchy. In fact, a substitution $P_H = 1$ in 4.31, 4.33, and 4.35 yields the correct result in this scenario.

For the anti-neutrino sector, the same calculations lead to

$$F_{\overline{\nu}_e} = P_{\overline{ee}}F^0_{\overline{\nu}_e} + (1 - P_{\overline{ee}})F^0_{\nu_x} \tag{4.36}$$

and

$$F_{\overline{\nu}_\mu} + F_{\overline{\nu}_\tau} = 2F_{\nu_x} = (1 - P_{\overline{ee}})F^0_{\overline{\nu}_e} + (1 + P_{\overline{ee}})F^0_{\nu_x} \tag{4.37}$$

where

$$P_{\overline{ee}} \equiv |U_{e1}|^2 P_H + |U_{e3}|^2(1 - P_H) \tag{4.38}$$

is the probability that an electron anti-neutrino produced in the SN is detected as such on Earth.

For a better understanding of the H/L-resonance, it is useful to take a look at Table 4.2 and the Figures 4.4 and 4.5. The non-adiabatic/adiabatic H-resonance in the anti-neutrino sector is shown for the case of inverted hierarchy.

	hierarchy	
	normal	inverted
small θ_{13}	ν-sector: adiab. res.	$\overline{\nu}$-sector: adiab. res.
large θ_{13}	ν-sector: non-adiab. res.	$\overline{\nu}$-sector: non-adiab. res.

Table 4.2: Occurrences and adiabaticity of the H-resonance in dependence on the mixing angle θ_{13}. Small θ_{13} means $\sin^2\theta_{13} \approx 10^{-6}$, large θ_{13} implies $\sin^2 2\theta_{13} \approx 0.2$.

In the non-adiabatic case (Figure 4.4) ($P_H = 1$, small θ_{13}), $\overline{\nu}_{3,m}$ and $\overline{\nu}_{1,m}$ mix maximally. Therefore, $F_{\overline{\nu}_1}$ has the original flux $F_{\overline{\nu}_e}$ when reaching Earth. Adding up the contributions $F_{\overline{\nu}_i}$ to the observable electron spectrum results in a harder spectrum than in the oscillation neglecting case.

In the adiabatic case (Figure 4.5) ($P_H = 0$, large θ_{13}), $\overline{\nu}_{3,m}$ and $\overline{\nu}_{1,m}$ do not mix. Therefore, $F_{\overline{\nu}_3}$ has the original $F_{\overline{\nu}_e}$ flux when reaching Earth. Compared to the non-adiabatic case, the $\overline{\nu}_e$ spectrum will be even harder, since it is to most part (1-$\sin^2\theta_{13}$) determined by the hard ν_x spectra, the original $\overline{\nu}_e$ hardly contributes.
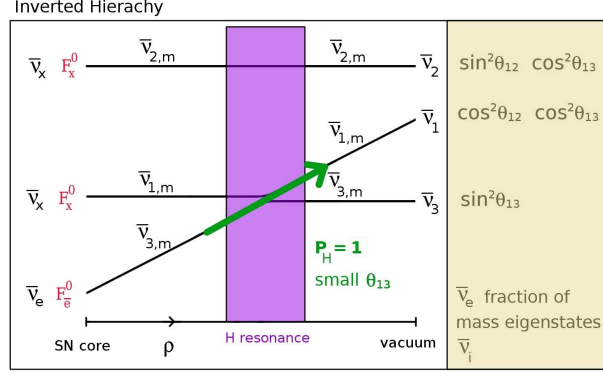
Figure 4.4: In case of inverted hierarchy, the H-resonance occurs in the anti-neutrino sector. The figure shows the evolution of the effective masses of the neutrino mass eigenstates with respect to the density. If θ_{13} is sufficiently small ($\sin^2\theta_{13} \approx 10^{-6}$), the resonance will be perfectly non-adiabatic and $P_H = 1$. Then, $\overline{\nu}_{1,m} \to \overline{\nu}_{3,m}$ and vice versa. The observed $\overline{\nu}_e$ spectrum on Earth, mainly determined by the spectra of $\overline{\nu}_1$ and $\overline{\nu}_2$, is harder than in the case without resonances and oscillation.

Figure 4.6 shows the dependence of the survival probabilities of ν_e and $\overline{\nu}_e$ on $\sin^2\theta_{13}$ for normal and inverted hierarchy and for different neutrino energies. For the inverted hierarchy and small θ_{13} ($\sin\theta_{13} \leq 10^{-6}$), the $\overline{\nu}_e$ survival probability $P_{\overline{ee}}$ is maximal, $\approx \cos^2\theta_{12} \approx 0.7$. The observed $\overline{\nu}_e$ spectrum on Earth will therefore match to a large extent ($\sim 70\%$) with the original $\overline{\nu}_e$ spectrum. For large θ_{13} ($\sin\theta_{13} \geq 10^{-3}$), the $\overline{\nu}_e$ survival probability $P_{\overline{ee}}$ is almost 0. As a result, the observed $\overline{\nu}_e$ spectrum on Earth will therefore be very similar to the original, hard $\overline{\nu}_x$ spectrum. The ν_e survival probability P_{ee} is almost constant, largely determined by the factor $\sin^2\theta_{12}$ and independent from P_H. Since the H-resonance appears in the neutrino sector in case of the normal hierarchy, only P_{ee} changes drastically with respect to θ_{13}, $P_{\overline{ee}}$ is almost constant, $\cos^2\theta_{12} \cos^2\theta_{13}$. Anyway, the observed ν_e spectrum on Earth will consist to a large extent of the original ν_x spectrum: In case of small θ_{13} the original ν_e flux contributes only 30%, for large θ_{13} it is completely negligible.

The outgoing shockwave reaches the resonance regions in $\mathcal{O}(1s)$ and can thus have an impact on the adiabaticity of the resonance. However, quan-
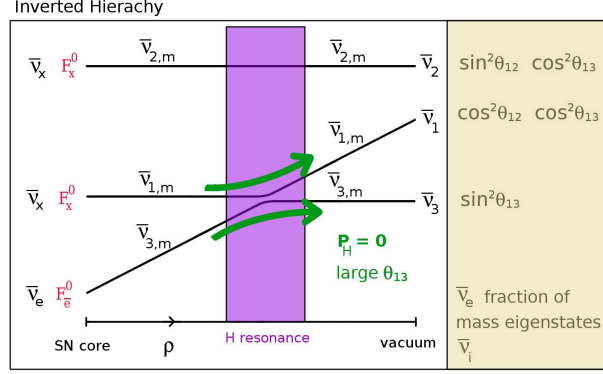
Figure 4.5: Analog to Figure 4.4, in case of adiabatic resonance. If θ_{13} is sufficiently large, the resonance will be perfectly adiabatic and $P_H = 0$. Then, $\overline{\nu}_{1,m}$ and $\overline{\nu}_{3,m}$ do not mix. The observed $\overline{\nu}_e$ spectrum on Earth, mainly determined by the spectra of $\overline{\nu}_1$ and $\overline{\nu}_2$, is even harder than for non-adiabatic-resonance.
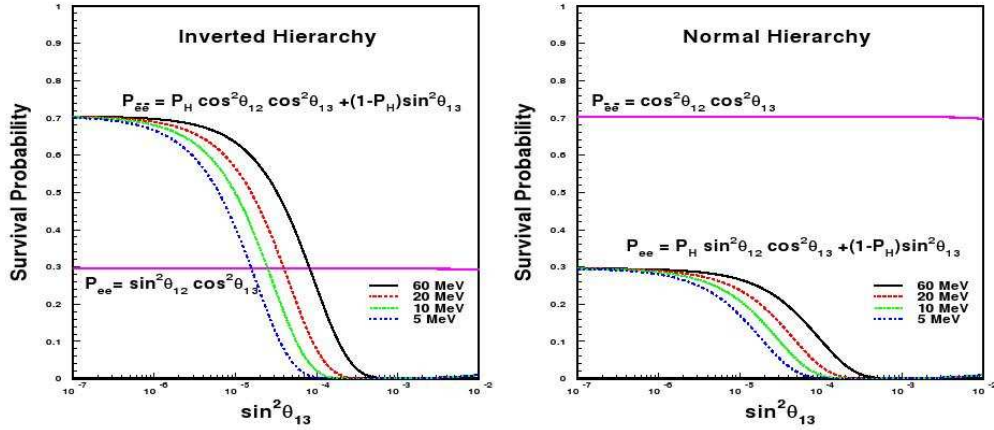

Figure 4.6: Dependence of the survival probabilities of ν_e and $\overline{\nu}_e$ on $\sin^2\theta_{13}$ for normal and inverted hierarchy and for different neutrino energies. Since the H-resonance occurs in the anti-neutrino sector for inverted hierarchy, only the $\overline{\nu}_e$ survival probability $P_{\overline{e}\overline{e}}$ depends on θ_{13} in this case. For the normal hierarchy, H-resonance appears in the neutrino sector and thus only the ν_e survival probability P_{ee} depends on θ_{13}. [60]

titative predictions are difficult and therefore not considered in the event rates calculations for LENA. If θ_{13} was sufficiently large ($\tan^2\theta_{13} > 10^{-5}$) and in case of inverted hierarchy, a shock wave effect could be seen in the anti-neutrino sector in the time-evolution of the average energies and the event rate. For further information on shock waves effect, see e.g. [61, 62]

4.5 Earth Matter Effect

The so-called Earth Matter Effect for SN neutrinos occurs when neutrinos coming from a SN pass through the Earth. Observation or non-observation of the effect can give further information on neutrino oscillation parameters and original fluxes.

The Earth Effect is usually expressed by the difference between the flux at the surface of the Earth F_e and the flux at the detector (on the opposite side of the Earth) $F_e^D = \sum_i P_{ie} F_i$, where P_{ie} denotes the probability that a ν_i entering the Earth reaches the detector as a ν_e.
Rewriting F_i again with the original fluxes F_α^0 one obtains

$$F_e^D - F_e = (1 - 2P_L)P_H(P_{2e} - |U_{2e}|^2)(F_e^0 - F_x^0), \qquad (4.39)$$

where $\sum_i P_{ie} = 1$ and $\sum_i |U_{ie}|^2 = 1$ was used. Due to the low density of the Earth ($\rho_E = \mathcal{O}(\text{g cm}^{-3})$) and the small mixing angle θ_{13}, the term proportional to $(P_{3e} - |U_{3e}|^2)$ can be neglected.

Evaluating the factor $(P_{2e} - |U_{2e}|^2)$, considering a constant density of the Earth and only a 2-flavour oscillations finally leads to the expression

$$\begin{aligned} F_e^D - F_e = \ & (1 - 2P_L)P_H \frac{\xi\sin^2 2\theta_{13}}{(\xi - \cos 2\theta_{13})^2 + \sin^2 2\theta_{13}} \\ & \times \sin^2(\frac{\pi z}{l_{osc,m}})(F_e^0 - F_x^0). \end{aligned} \qquad (4.40)$$

The expression also holds for $\overline{\nu}_e$, setting P_L to 1. The dimensionless density parameter ξ is the same as in Eq. (4.22) and z denotes the distance the neutrino travelled trough the Earth. The oscillation length in matter $l_{osc,m}$ is the defined in Eq. (4.23) and can be rewritten to

$$l_{osc,m} = 3.1 \cdot 10^2 \text{ km} \frac{1}{\sqrt{\xi - \cos 2\theta_{13})^2 + \sin^2 2\theta_{12}}} \left(\frac{E}{10\text{MeV}}\right) \left(\frac{8 \cdot 10^{-5}\text{eV}^2}{\Delta m_{12}^2}\right). \qquad (4.41)$$

From Eq. (4.40) the conditions for the appearance of the Earth Effect can be derived. First, there has to be a difference of the original fluxes F_e^0 and F_x^0. This condition is satisfied according to recent SN models [42, 41, 40], which predict different spectral shapes for ν_e and ν_x as explained in Chapter 3. Second, there has to be as well a difference between F_1 and F_2 at Earth, while the third generation is neglected. In Eq. (4.40), this is considered in the factor $(1 - 2P_L)P_H$: if $P_H = 0$, $F_1 = F_2 = F_x^0$, and if $P_L = 1/2$, $F_1 = F_2 =$ have the same mixture of the original spectra of ν_e and ν_x. As a result, there is no Earth Effect for neutrinos (anti-neutrinos) for normal (inverted) hierarchy, if the H-resonance is adiabatic. Table 4.3 shows in which scenarios the Earth Effect appears.

	small θ_{13}	large θ_{13}
normal hierarchy	$\nu_e, \overline{\nu}_e$	$\overline{\nu}_e$
inverted hierarchy	$\nu_e, \overline{\nu}_e$	ν_e

Table 4.3: Occurrences of the Earth Effect for ν_e and $\overline{\nu}_e$ for different scenarios. Small and large θ_{13} describe a non-adiabatic and adiabatic H-resonance, respectively.

Implications of the Earth Effect on the observed signal of a single detector have been investigated closely by A. Dighe *et al.* [63]. Figure 4.7 shows the impact of the Earth Effect on the observed SN-ν spectrum in LENA (charged current reaction of $\overline{\nu}_e$ on protons), under the assumption of a constant density of the Earth and neglecting the energy resolution of the detector. Characteristic for the Earth Effect are the modulations in the spectrum due to the term $\sin^2(\frac{\pi z}{l_{osc,m}})$, so-called "wiggles".

With the $\overline{\nu}_e$ capture on protons (compare Chapter 5) LENA provides the possibility to investigate the Earth Effect with high statistics. In case of an observation of wiggles, a precise model independent measurement of θ_{12} is possible (compare Eq. (4.40)). On the other hand, in case of a non-observation, θ_{13} is constrained to be large and the hierarchy must be inverted (see Table 4.3).

It is noteworthy, that if θ_{13} is small ($\sin^2\theta_{13} \approx 10^{-6}$), the observation of the Earth Effect of SN-ν might be the only possibility to obtain information on this mixing angle.
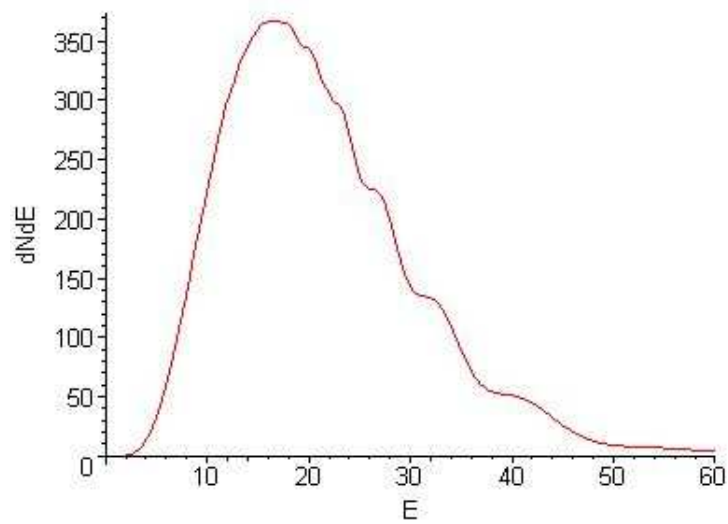
Figure 4.7: Event rate per energy bin of the inverse beta decay, considering the Earth Effect. Typical are the oscillations, so-called wiggles, in the decline of the curve, that can be observed in a single detector if the energy resolution is sufficient. Further information on the detection of the Earth Matter Effect in a single detector can be found in [63].

Chapter 5

SN Event Rates

The observation of a galactic SN-ν can deliver valuable information on the total ν flux and single fluxes. Spectroscopy allows implications on the average ν energies. Different mixing scenarios might be differed leading to constraints on intrinsic neutrino parameters. Due to the high statistics, even a time-resolved neutrino flux rate for different neutrino interactions could be measured and thus give new information on the dynamics of supernova explosions.

Overall, eight different channels have been investigated in the event rate calculations for SN neutrinos in LENA. The most dominant channel is the capture of $\overline{\nu}_e$ on protons. Furthermore, elastic scattering on protons and electrons, and charged current (CC) and neutral current (NC) reactions on ^{12}C and ^{13}C are considered. An advantage for the detection and separation of the different channels is that LENA has a very low energy threshold and due to a light yield of $\sim 10^2$ pe[1]/MeV a very good energy resolution. In addition the possibility to separate reaction channels is given by measuring delayed coincidence signals.

Even if a galactic supernova (SN) is optically hidden, the LENA detector is capable to observe it with high statistics by means of its emitted neutrinos. For a standard supernova scenario, about $1.5 \cdot 10^4$ events are expected within 10 s. However, as LENA is a fast scintillation detector, they can still be separated in time. Anyway, for these rare cases spatial reconstruction can be applied to differ between the simultaneous events (see Chapter 7).

---

[1]photo electrons

5.1 Reactions Channels in LENA

A detailed discussion of the eight reaction channels under invesigation for
the detection of SN neutrinos in LENA is presented in this section. Cross-
section, energy threshold, and signature are pointed out for every channel.

The channels are classified into charged current (CC) and neutral current
(NC) interactions. Whereas CC reactions are only possible for electron type
neutrinos, NC reactions are possible for all flavours. The energy dependence
of all cross-sections (except elastic scattering on protons) is shown in Figure
5.2.

5.1.1 Charged Current Interactions

The CC reaction channels can be used to both investigate the ν_e and $\overline{\nu}_e$ flu-
ence. Spectroscopy can be used to determine the average neutrino energies.

1. **Inverse beta decay**

$$\overline{\nu}_e + p \to n + e^+ \tag{5.1}$$

   The energy threshold of this reaction is $E_{thr} = 1.80$ MeV. For the cross-
   section, the first order approximation $\sigma_{inv\beta} \approx 9.5 \cdot 10^{-44} \, (E_\nu/\text{MeV} -
   1.29)^2$ cm^2 [64] has been used for the event rate calculations.
   The channel can be clearly identified in a liquid scintillator detector
   like LENA due to the delayed coincidence of the positron and the 2.2
   MeV γ from neutron capture on protons,

$$n + p \to d + \gamma, \tag{5.2}$$

   with a mean capture time of $\tau \approx 250$ μs.

   The inverse beta decay provides the highest statistics among all chan-
   nels, due to the low energy threshold and the largest cross-section of
   all channels (see Figure 5.2).

2. **CC capture of $\overline{\nu}_e$ on ^{12}C**

$$\overline{\nu}_e + {}^{12}\text{C} \to {}^{12}\text{B} + e^+ \tag{5.3}$$

   The energy threshold of this reaction is 14.39 MeV. The cross-section
   has been obtained by a fit to data from [65]. ^{12}B redecays with a
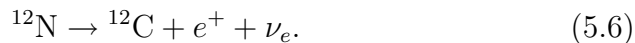   lifetime of $\tau = 20.20$ ms:

$$^{12}\text{B} \rightarrow {}^{12}\text{C} + e^- + \overline{\nu}_e. \tag{5.4}$$
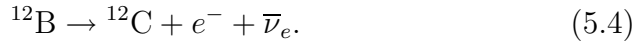
The reaction can be tagged with the help of the delayed coincidence of the positron and the electron.

3. **CC capture of ν_e on ^{12}C**

$$\nu_e + {}^{12}\text{C} \rightarrow {}^{12}\text{N} + e^- \tag{5.5}$$

Subsequently,

$$^{12}\text{N} \rightarrow {}^{12}\text{C} + e^+ + \nu_e. \tag{5.6}$$

^{12}N has a lifetime of $\tau = 11.00$ ms.
The cross-section was obtained with a linear spline interpolation to data given in [65]. Due to the relatively high energy threshold, $E_{thr} = 17.34$ MeV, statistics are limited. Nonetheless, this reaction is the most important for the determination of the ν_e flux.

The CC reaction of ν_e on carbon and the subsequent decay of ^{12}N give a clear delayed coincidence signal, but so does the channel $\overline{\nu}_e + {}^{12}\text{C} \rightarrow {}^{12}\text{B} + e^+$. Both have comparable decay times of $\tau_{^{12}\text{N}} = 11.00$ ms and $\tau_{^{12}\text{B}} = 20.20$ ms, making a separation difficult.

Still, the ν_e flux can be determined, subtracting the $\overline{\nu}_e$ flux from the observed common flux of the CC reactions on Carbon. The $\overline{\nu}_e$ flux can be measured independently in the inverse beta decay with a precision of about 2%. The error on the cross-section of the CC capture on Carbon of $\overline{\nu}_e$ is $\sim$10% [65]; it is the main contribution to the uncertainty of the ν_e flux of $\sim$50%.

4. **CC capture of ν_e on ^{13}C**

$$\nu_e + {}^{13}\text{C} \rightarrow {}^{13}\text{N} + e^- \tag{5.7}$$

The natural abundance, and therefore the abundance in the liquid scintillator, of ^{13}C is only about 1%. However, due to the low energy threshold, $E_{thr} = 2.22$ MeV, and the high cross-section [66, 67] this channel can provide valuable information on ν_e.

Again, the signature is a delayed coincidence of an electron with the positron from the decay of ^{13}N,

$$^{13}\text{N} \rightarrow {}^{13}\text{C} + e^+ + \nu_e. \tag{5.8}$$

The lifetime of ^{13}N is high, $\tau = 862$ s, what makes an observation of the delayed coincidence between electron and positron rather complicated. The required long time window increases the probability for random coincidences drastically, which has to be taken into account for the analysis. However, the detection efficiency has been set to 1 in the event rate calculations.

5.1.2   Neutral Current Interactions

NC reaction channels provide valuable, complementary information on the total and $^\langle \overline{\nu}_x{}^\rangle$ $(x = \mu, \tau)$ fluxes.

1. **NC scattering on ^{12}C**

$$\nu + {}^{12}\text{C} \rightarrow {}^{12}\text{C}^* + \nu \tag{5.9}$$

The decay of the excited state $^{12}\text{C}^*$,

$$^{12}\text{C}^* \rightarrow {}^{12}\text{C} + \gamma, \tag{5.10}$$

leads to the emission of a mono-energetic 15.11 MeV γ. Thanks to the high energy resolution in liquid scintillator, this channel can be easily seperated from the others. Due to its high statistics, the NC scattering on ^{12}C is very important for the determination of the overall flux. The cross-section was obtained from a linear spline interpolation of data given in [65].

2. **Elastic scattering on electrons**

$$\nu + e^- \rightarrow \nu + e^- \tag{5.11}$$

This channel is sensitive to all neutrinos and anti-neutrinos; however, the cross-sections for ν_e and $\overline{\nu}_e$ are higher due to the contribution of CC interactions. All cross sections are proportional to the neutrino energy in the energy regime of interest [64].

$$\sigma_{\nu_e} = 9.2 \cdot 10^{-45} \frac{E}{\text{MeV}} \text{cm}^2 \tag{5.12}$$

$$\sigma_{\overline{\nu}_e} = 3.83 \cdot 10^{-45} \frac{E}{\text{MeV}} \text{cm}^2 \tag{5.13}$$

$$\sigma_{\nu_x} = 1.57 \cdot 10^{-45} \frac{E}{\text{MeV}} \text{cm}^2 \tag{5.14}$$

$$\sigma_{\overline{\nu}_x} = 1.29 \cdot 10^{-45} \frac{E}{\text{MeV}} \text{cm}^2 \tag{5.15}$$

The energy threshold of this channel in LENA depends on the radio-purity of the scintillator, the definition of the fiducial volume, and the PMT dark noise. Event rates have been calculated for $E_{thr} = 0.2$ MeV and $E_{thr} = 0.4$ MeV. However, no significant difference occurred in the calculated rates due to the small flux contributions at low energies.

3. **Elastic scattering on protons**

$$\nu + p \rightarrow \nu + p \tag{5.16}$$

This important channel for the LENA detector has first been investigated by J.F. Beacom *et al.* [68]. It provides the second highest statistics of all channels, however the actual number of events is very sensitive to the energy threshold of the detector. The cross-section for this reaction has been taken from [69, 70, 71]. For the energy threshold, the same statements hold as for the elastic scattering on electrons.

Event rate calculations for the elastic scattering on protons have to take into account that the recoil protons are quenched. This means that the scintillation light output is lower with respect to an electron with the same energy. Quenching is described by the semi-empirical Birks' formula [73]

$$\frac{dE_{equiv}}{dx} = \frac{A \frac{dE}{dx}}{1 + k \frac{dE}{dx}}, \tag{5.17}$$

where $\frac{dE_{equiv}}{dx}$ is the light output per unit lenght with respect to an electron, $\frac{dE}{dx}$ the energy loss according to the Bethe-Bloch law, A the absolute scintillation efficiency, and k a parameter relating the density of ionisation centres to $\frac{dE}{dx}$. In the calculations, k was set to $1.5 \cdot$

10^{-3} cm MeV^{-1}, a value obtained in measurements for PXE in the Counting Test Facility (CTF) [74] for Borexino. Due to the quenching, low energetic recoils and thus signals from elastic scattering of low energy neutrinos are suppressed. The proton elastic scattering channel is therefore mostly sensitive to the μ- and τ-neutrinos, if no oscillations occur. ν_e and $\overline{\nu}_e$ make up only about 15% of the number of detected events in this scenario.

From Eq. (5.17) follows with $A = 1$

$$E_{equiv}(T_p) = \int_0^{T_p} \frac{dE}{1 + k\frac{dE}{dx}}, \qquad (5.18)$$

where T_p denotes the proton recoil energy. The quenched proton recoil spectrum $\frac{dN}{dE_{equiv}}$ can be derived from the unquenched proton spectrum $\frac{dN}{dT_p}$ to

$$\frac{dN}{dE_{equiv}} = \frac{dN}{dT_p} \frac{dT_p}{dE_{equiv}}. \qquad (5.19)$$

Figure 5.1 shows quenched proton recoil spectra for the KRJ model. The main contribution to this channel comes, in the case of no oscillations, from μ- and τ-neutrinos.

4. NC scattering on ^{13}C

$$\nu + {}^{13}\text{C} \rightarrow {}^{13}\text{C}^* + \nu \qquad (5.20)$$

From the deexcitation of ^{13}C* a monoenergetic 3.68 MeV γ is emitted, giving a separable signal.

$$^{13}\text{C}^* \rightarrow {}^{13}\text{C} + \gamma. \qquad (5.21)$$

Like the NC scattering on ^{12}C, this channel offers the possibility to measure the total SN-ν flux.

Despite the small ^{13}C abundance of only 1% in natural Carbon, a detection is feasible in LENA. This is due to a much lower energy threshold of 3.68 Mev and a higher cross-section [66] below ~ 20 MeV in comparison to the NC scattering on ^{12}C.
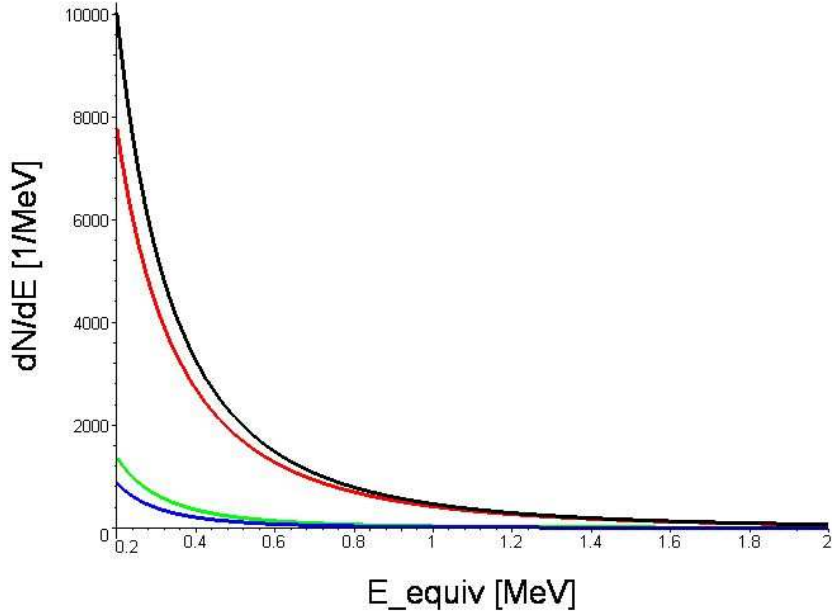
Figure 5.1: Quenched proton spectrum as a function of the energy, for the SN model from KRJ [41] neglecting oscillation. Black: all flavours. Red: $\overset{\scriptscriptstyle(}{\overline{\nu}}\overset{\scriptscriptstyle)}{}_x$ ($x = \mu, \tau$). Green: $\overline{\nu}_e$. Blue: ν_e. The contribution from $\overset{\scriptscriptstyle(}{\overline{\nu}_x}\overset{\scriptscriptstyle)}{}$ ($x = \mu, \tau$) to the total rate is dominant, allowing an approximate determination of F_x in a direct measurement.

5.2   Calculation of Event Rates

The number of events N_{events} can be calculated as follows, neglecting the finite energy resolution of the detector:

$$N_{event} = \int_{E_{thr}} F_\alpha(E) \; \sigma(E) \; N_p \; dE, \tag{5.22}$$

where $F_\alpha(E)$ denotes the neutrino spectrum at Earth, $\sigma(E)$ the cross-section for the involved reaction and N_p the number of targets in LENA, depending on the liquid scintillator and fiducial volume. For the calculations, the fiducial volume is defined as in Chapter 2, and it is assumed to be filled with the liquid scintillator PXE. The rates for the alternative scintillator LAB can easily be calculated with the help of the factors given in Table 5.1.

All channels have been investigated for three different SN simulation models: Lawrence-Livermore (LL) [40], Thompson, Burrows, and Pinto (TBP)
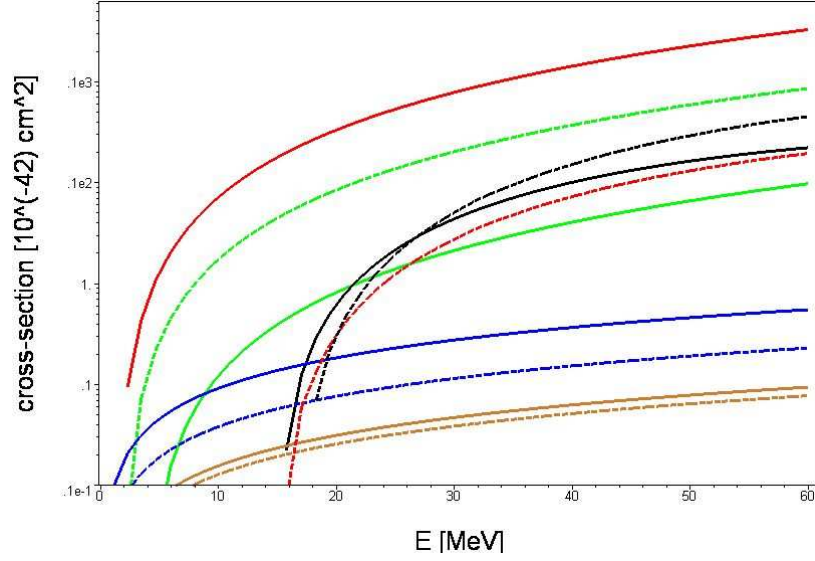
Figure 5.2: Cross-sections as a function of energy for different channels for SN-ν detection in LENA. Solid red line: inverse beta decay; dashed red line: NC on ^{12}C. Solid green line: NC on ^{13}C; dashed green line: CC on ^{13}C. Solid black line: CC of $\overline{\nu}_e$ on ^{12}C; dashed black line: CC of ν_e on ^{12}C. Solid blue line: ν_e-e scattering, dashed blue line: $\overline{\nu}_e$-e scattering. Solid yellow line: ν_x-e scattering, dashed yellow line: $\overline{\nu}_x$-e scattering.

target particle	PXE	LAB
H	1	1.25
e^-	1	0.91
C	1	0.85

Table 5.1: Factors for the calculation of event rates for scintillator LAB with respect to PXE. Reactions on p are enhanced, while the other channels have less statistic than for PXE.

[42], and Keil, Raffelt, and Janka (KRJ) [41]. The differences of the three SN models under investigation are shown in Table 5.2 considering average energies and pinching factors η. For a non-pinched thermal spectrum $\langle E_\alpha \rangle = 3.15\ T_\alpha$ holds.

Assuming an energy equipartition between all flavours, the number lumi-

SN model	$\langle E_e \rangle$ [MeV]	η_e	$\langle E_{\overline{e}} \rangle$ [MeV]	η_e	$\langle E_x \rangle$ [MeV]	η_x
LL	12.0	0	15.4	0	21.6	0
KRJ	13.0	2.1	15.4	3.2	15.7	0.8
TBP	10.0	0	11.4	0	14.1	0

Table 5.2: Comparison of mean energies of three SN models: Lawrence-Livermore (LL) [40], Keil, Raffelt, and Janka (KRJ) [41], and Thompson, Burrows, and Pinto (TBP) [42]. Especially the average energies of μ and τ-ν show a distinct hierarchy depending on the model itself: $\langle E_x^{LL} \rangle > \langle E_x^{KRJ} \rangle > \langle E_x^{TBP} \rangle$. Pinching factors η only occur in the model of KRJ (see Chapter 4).

nosities L_α are

$$L_\alpha = \frac{E_B/6}{\langle E_\alpha \rangle}, \tag{5.23}$$

where a total energy released in the explosion $E_B = 3 \cdot 10^{53}$ erg was used in the event rate calculations.

The big differences between the SN models and other uncertainties that enter the event rate calculations, e.g. the oscillation scenario, make it difficult to predict exact rates. Therefore, an order of magnitude estimation for the event rates of the eight channels is made to give an idea of the contributions of each channel. An overview of the average rates for all channels is given in Table 5.3. Neglecting resonances and assuming $E_{thr} = 0.4$ MeV for the elastic scattering channels, a total event rate of $\sim 1.4 \cdot 10^4$ is expected. For the sake of completeness, the sensitivity to the neutrino flavours of each channel is shown.

5.3 Results

The resulting event rates calculated for 8 possible channels in LENA for different SN models and neutrino parameter scenarios are summarised in Table 5.5. The scenario of no oscillation has been considered as well as L- and H-resonance (see Chapter 4). Input parameters were chosen according to Eq. (4.16). The large θ_{13} refers to the upper limit measured by CHOOZ [19], $\sin^2 2\theta_{13} \approx 0.2$, the small θ_{13} has been set to $\sin^2 \theta_{13} \approx 10^{-6}$.

An important result of the rate calculations shown in Table 5.5 is the

channel	average rate [no resonance]	flux information
$\overline{\nu}_e p \rightarrow n\ e^+$	9,200	$F_{\overline{e}}$
$\overline{\nu}_e\ {}^{12}\mathrm{C} \rightarrow {}^{12}\mathrm{B}\ e^+$	250	$F_e + F_{\overline{e}}$
$\nu_e\ {}^{12}\mathrm{C} \rightarrow {}^{12}\mathrm{N}\ e^-$	500	
$\nu_e\ {}^{13}\mathrm{C} \rightarrow {}^{13}\mathrm{N}\ e^-$	$\mathcal{O}(10)$	F_e
$\nu\ {}^{12}\mathrm{C} \rightarrow {}^{12}\mathrm{C}^*\nu$	1,250	F_{tot}
$\nu e^- \rightarrow \nu e^-$	700	F_{tot}
$\nu p \rightarrow \nu p$	2,350	F_x
$\nu\ {}^{13}\mathrm{C} \rightarrow {}^{13}\mathrm{C}^*\nu$	$\mathcal{O}(10)$	F_{tot}
total	14,250	

Table 5.3: Average event rates for SN-ν from thermal production in LENA along with the flux that can be measured by each channel. For the CC reaction on ^{12}C, both fluxes are given, as they are measured together. $E_{thr} = 0.4$ MeV, normal hierarchy, no resonances (corresponding to perfectly adiabatic H- and L-resonance) are assumed. The signal rates for reactions on ^{13}C are low, however the statistics would rise for a SN closer than 10 kpc.

hierarchy of the event rates for the three SN models. This is closely linked to the hierarchy of the average energies of μ- and τ-neutrinos (see Table 5.2). Higher average energies produce harder spectra which results in higher event rates since the cross-sections increase with increasing energy. However, according to Eq. (5.23), the total flux decreases at the same time.

H- and L- resonances in the supernova (see Chapter 4) do not have an impact on the event rates of the NC channels. This is due to the equal cross-sections for all flavours for NC scattering on Carbon and for elastic scattering on protons and the fact that oscillations into so-called sterile neutrinos are not considered in this thesis. Recent limits on sterile ν can be found in [23]. Note that the independence of oscillations allows a distinction between the different SN models from the measurement of the NC channels.

Concerning the event rates for ν_e and $\overline{\nu}_e$, there is a noticeable hierarchy regarding the different neutrino oscillation scenarios. First of all, the event rates for electron-type neutrinos in the case of no oscillation are least. If resonances occur, the original, harder $\overset{(-)}{\nu}_x$ spectrum will contribute to the observed ν_e or $\overline{\nu}_e$ spectrum on Earth. As all cross-sections increase with increasing energy, a higher event rate is detectable.

In order to compare the three oscillation scenarios, it is helpful to remind oneself of the Figures 4.2, 4.3, 4.4, and 4.5 and the Equations (4.33), (4.34), (4.36), and (4.38) in Chapter 4.

For the CC reactions of ν_e on Carbon, in the case of a small θ_{13} and any hierarchy (further denoted as s/a), a ν_e produced in the SN will arrive at Earth as ν_2. The survival probability of a ν_e is in both cases $P_{ee} \approx 0.31$ and thus the event rates are equal.

Also, in the case of a large θ_{13} and inverted hierarchy (l/i), the original ν_e flux will be identical to the ν_2 flux on Earth. However, since the mixing angle is larger, the survival probability $P_{ee} \approx 0.29$ is slightly smaller, as $P_{ee} \propto \cos^2\theta_{13}$ Therefore, there is a larger contribution of the hard ν_x spectrum to the ν_e spectrum at Earth and thus more events can be expected.

For normal hierarchy and large θ_{13} (l/n), the event rate is highest. The contribution from the original ν_e flux to the flux measured on Earth is neglible, $P_{ee} \approx 0.05$. Therefore, the ν_e spectrum is hardest in this case.

Analogously, it is possible to consider the implications of resonances on the $\overline{\nu}_e$ flux observed on Earth. The hierarchy is more distinct for the inverse beta reaction than for the CC reaction on ^{12}C because of the higher statistics.

In case of small θ_{13} and normal hierarchy (s/a), $P_{\overline{ee}} \approx 0.69$. A $\overline{\nu}_e$ produced in the core, identical to $\overline{\nu}_{3,m}$ for inverted hierarchy and $\overline{\nu}_1$ for normal hierarchy, arrives in both cases at Earth as $\overline{\nu}_1$.

In case of normal hierarchy and large θ_{13} (l/n), no resonance occurs and an initial $\overline{\nu}_e$ will arrive on Earth as $\overline{\nu}_1$ as well. However, the difference in θ_{13} slightly reduces the contribution from the original soft SN-$\overline{\nu}_e$ spectrum, $P_{\overline{ee}} \approx 0.65$.

Most events can be observed in the case of large θ_{13} and inverted hierarchy (l/i). The survival probability $P_{\overline{ee}} \approx 0.05$ is small and the contributions from the hard SN-$\overline{\nu}_x$ spectrum to the $\overline{\nu}_e$ spectrum are large. Combined with the information on the SN models from the NC channels, neutrino oscillation parameters could be deduced.

In case θ_{13} is below the sensitivity of future experiments like Double Chooz [75] or Daya Bay [76], the observation of a SN would provide valuable

- possibly unique - information on θ_{13}.

Rates for the neutronisation burst are listed in Table 5.4 for all the channels sensitive to ν_e, except reactions on ^{13}C. The time-dependent spectra of luminosity and average energy were taken from T.A. Thompson *et al.* [42]. Assuming a thermal spectrum with a temperature $T_\alpha = \frac{\langle E_\alpha(t) \rangle}{3.15}$ at time t, the time-resolved neutrino fluence can be calculated according to Eq. (5.22). The event rate was finally obtained by integration over time.

Information on SN parameters and constraints on the neutrino masses can be investigated with the help of the detection of ν_e from the neutronisation burst model independently. The observation/non-observation of the neutronisation burst ν_e in the different channels also allows implications on the H-resonance and the mass hierarchy. While the channels sensitive to all flavours definitely see the neutronisation burst, its observation in the inverse beta decay depends on the oscillation scenario.

channel	events
$\nu_e {}^{12}\text{C} \rightarrow {}^{12}\text{N } e^-$	7
$\nu_e {}^{12}\text{C} \rightarrow {}^{12}\text{C}^* \nu_e$	14
$\nu_e e^- \rightarrow \nu_e e^-$	27
$\nu_e p \rightarrow \nu_e p$	26
total	74

Table 5.4: Event rates for ν_e from neutronization burst neglecting neutrino oscillations.

channel	TBP				KRJ				LL			
	no osc.	s/a	l/n	l/i	no osc.	s/a	l/n	l/i	no osc.	s/a	l/n	l/i
$\overline{\nu}_e p \to n\, e^+$	6806	7494	7463	8606	8737	9022	9058	9606	9631	10993	11170	13793
$\overline{\nu}_e\,^{12}\text{C} \to {}^{12}\text{B}\, e^+$	110	149	149	221	200	228	232	285	293	398	411	612
$\nu_e\,^{12}\text{C} \to {}^{12}\text{N}\, e^-$	59	197	248	201	129	277	332	281	137	674	874	690
$\nu_e\,^{13}\text{C} \to {}^{13}\text{N}\, e^-$	14	19	21	19	18	22	23	22	17	29	34	29
$\nu\,^{12}\text{C} \to {}^{12}\text{C}^*\nu$	684	684	684	684	950	950	950	950	2073	2073	2073	2073
$\nu e^- \to \nu e^-$ [1]	684	684	684	684	684	684	684	684	684	684	684	684
$\nu p \to \nu p$ [1]	1469	1469	1469	1469	2138	2138	2138	2138	5740	5740	5740	5740
$\nu p \to \nu p$ [2]	621	621	621	621	968	968	968	968	3414	3414	3414	3414
$\nu\,^{13}\text{C} \to {}^{13}\text{C}^*\nu$	11	11	11	11	13	13	13	13	19	19	19	19
total [1]	9837	10707	10729	11895	12869	13334	13430	14079	18594	20610	21005	23640
total [2]	8989	9859	9881	11047	11699	12146	12260	12909	16267	18284	18679	21314

Table 5.5: Event rates for SN-ν from thermal production in LENA, for different SN models (TBP [42], KRJ [41], and LL [40]) and different oscillation scenarios. For each model, four cases are considered: 1. (no osc), case of no oscillation, 2. (s/a), small mixing angle θ_{13} and any hierarchy, 3. (l/n), large θ_{13} and normal hierarchy, and 4. (l/i), large θ_{13} and inverted hierarchy. The large θ_{13} refers to the upper limit measured by CHOOZ [19], $\sin^2 2\theta_{13} \approx 0.2$, the small θ_{13} has been set to $\sin^2 \theta_{13} \approx 10^{-6}$.
In total, the total event rate differs between $1.0 - 1.9 \cdot 10^4$ events for no-oscillation and $1.2 - 2.4 \cdot 10^4$ for (l/i) for the different models, assuming an energy threshold of 0.2 MeV for the elastic scattering processes. For an $E_{thr} = 0.4$, the total event rates vary between $0.9 - 2.1 \cdot 10^4$.

[1] $E_{thr} = 0.2$ MeV
[2] $E_{thr} = 0.4$ MeV

Chapter 6

Light Yield Measurement

The light yield of the liquid scintillator is an important quantity for experiments like LENA, since it is closely linked to the spatial as well as the energy resolution of the detector. The light yield describes the number of photons emitted by the scintillator per amount of energy deposited by an ionizing particle. It can also be denoted as the number of photoelectrons seen by all photomultipliers of a given experiment as a function of the energy deposition.

The measurement of the absolute light yield is difficult, since it requires a 4π geometry and precise knowledge of the detector efficiency [77]. Therefore, a measurement of the relative light yield is presented in this Chapter. A calibration is provided by measurements of M. Wurm [50] based on experiments at the CTF for Borexino [78] and by C. Buck in Heidelberg [79]. In the CTF the light yield of a PXE based scintillator was determined to be 372 ± 8 pe[1]/MeV.

In the first section of this chapter, an overview about scintillation physics and the solvents and fluors under investigation is provided. The experimental setup and the readout electronics are presented in the subsequent sections. Results of the measurements and a discussion follow in the last section.

6.1   About Liquid Scintillators

Liquid scintillator has many properties that make it especially suited for a multipurpose detector like LENA. First of all, it both serves as target for incident particles and as source of scintillation light that can be detected with photomultipliers. Liquid scintillators provide an excellent energy resolution

---

[1]photo electrons

and a low energy threshold, making spectroscopy of low energy particles feasible. Moreover, the fast scintillation decay times allow to distinguish between events that happen within a short time scale of $\mathscr{O}(10\ \text{ns})$.

Organic liquid scintillators are aromatic hydrocarbon compounds containing benzene-ring structures. Passing particles deposit ionizing energy in the scintillator, exciting the free valence electrons of the benzene rings. Scintillation light is emitted due to transitions from excited states to the ground state. Since singlet states decay faster than triplet states, a fast (3-4 ns) and a slow (~ 20 ns) decay component of the scintillation light can be observed.

Due to the overlap of the optical absorption and emission band of its molecules, the solvent is in general not transparent for its own scintillation light. Therefore, wavelength shifters (also denoted as fluors) are added in small concentrations of a few g/ℓ. Their purpose is to absorb the scintillation light and re-emit it at higher wavelengths where the solvent is transparent.

Several quantities determine whether a scintillator is suited for an experiment. Light scattering and absorption reduce the average distance the scintillation light is able to propagate. The attenuation length, combining these two quantities, therefore determines to a large extent the size of the detector. Moreover, in order to be able to apply pulse shape discrimination for the distinction between different types of particles, fast scintillation decay times are preferred. They are also important for a good spatial event reconstruction.

The effective light yield of an organic liquid scintillator depends largely on the solvent and the fluor(s) in use. First it depends on the light yield of the solvent and the fluor themselves, second on the efficiency of the energy transfer from the solvent to the fluor (i.e. the overlap of the emission band of the solvent and the absorption band of the fluor), and third on the emission wavelength of the fluor. If the wavelength is larger, light absorption by the solvent is less important and the light yield is higher.

A possible solvent for LENA is Phenyl-o-Xylylethane (PXE, $C_{16}H_{18}$; see Figure 6.1 for the the chemical structure). Its relatively high density $\rho_{PXE} = 0.985$ g cm^{-3} supports the self-shielding of the scintillator against external background. Moreover, since current studies imply a water-filled outer muon veto, the small difference in the densities of both materials would minimize buoyant forces. PXE itself mainly emits around a wavelength of 290 nm. However, it is necessary to shift the scintillation light to $\approx$430 nm

in order to obtain an attenuation length > 10 m for PXE. This rather large wavelength shift can be either achieved using a combination of PPO/pTP and bisMSB as fluors, or with PMP. Additionally, PXE has to be purged in an Al_2O_3-column [78].
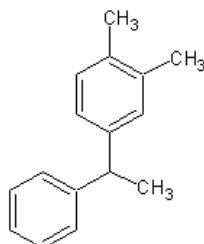

Figure 6.1: Chemical structure of PXE.

Another promising liquid scintillator is Linear Alkylbenzene (LAB, CH_3- $(CH_2)_n-CH(C_6H_5)-(CH_2)_m-CH_3$, n+m =7-10) with a lower density than PXE, $\rho_{LAB} = 0.863$ g cm^{-3}. The emission band of LAB is around 280 nm. Like PXE, the attenuation length is > 10 m at 430 nm. Figure 6.2 shows the chemical structure of LAB.
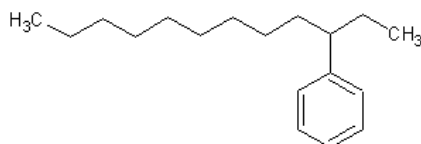
Figure 6.2: Chemical structure of LAB for n=8 and m=1.

As already mentioned, wavelength shifters are an indispensable component for the liquid scintillators allowing the scintillation light to reach the PMTs. Several fluors are currently under investigation for scintillator mixtures that might be used in the LENA detector: 2,5-Diphenyloxazole (PPO), para-Terphenyl (pTP), 1-Phenyl-3-Mesityl-2-Pyrazolin (PMP), and 1,4-bis-(o-methylstyryl)-benzole (bisMSB). Their chemical structure, absorption and emission bands are listed in Table 6.1.

For the fluors, primary and secondary wavelength shifters are distinguished. Primary shifters absorb the scintillation light from the solvent, while a secondary shifter can be added in order to shift the emitted light from the primary further. As a result, the effective light yield will be higher
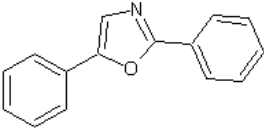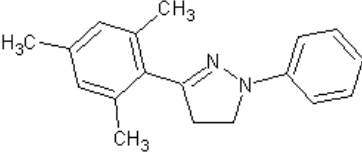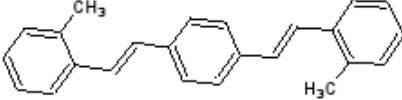
fluor	structure	absorption [nm]	emission [nm]
PPO		280-325	350-400
pTP		250-300	320-370
PMP		around 290	around 410
bisMSB		320-370	380-450

Table 6.1: Comparison of absorption and emission lines of several fluors considered for use in LENA, along with their chemical structure.

because the attenuation length increases for larger wavelengths and thus more photons reach the PMTs. While PPO, PMP and pTP are primary fluors, bisMSB is a secondary fluor. PMP is special, since it already emits at a high wavelength and thus fulfills the task that is usually done by the combination of two fluors. This type of wavelength shifter is referred to as high Stoke's shift fluor.

The measurement described in this Chapter puts the focus on PMP as a fluor and LAB as a solvent, since their application in a liquid scintillator detector has been considered only recently. Investigations on LAB have also been done for the SNO+ detector [80], the planned successor of the SNO detector that is supposed to be filled with liquid-scintillator instead of heavy water.

6.2 Setup

For the determination of the relative light yield of different liquid scintillators, a coincidence measurement has been set up. Monoenergetic γ particles emitted from a ^{137}Cs source are used to excite the molecules of a liquid scintillator sample that emit scintillation light. Whereas the scintillation light is collected with a PMT, the scattered γ is detected in a NaJ crystal. A coincidence between PMT and NaJ helps to effectively suppress background. Choosing the positions of source, scintillator probe and NaJ, thus constraining the scattering angle θ of the γ, only depositions of a fixed energy are recorded.

The energy E_{dep} of the Compton electron, and thus the energy deposition in the scintillator is

$$E_{dep} = E_0 - \frac{E_0}{1 + \frac{E_0}{m_e}(1 - \cos\theta)}. \tag{6.1}$$

E_0 is the energy of the initial γ, $m_e = 511$ keV denotes the electron mass.

In the specific case of a scattering angle $\theta = 180°$ and a 662 keV γ from the ^{137}Cs source ($\sim$330 kBq), the energy deposition is 478 keV. Considering the finite width of the scintillator sample and the NaJ, a coincidence is still possible for a scattering angle of 162°, which is equivalent to a reduction of 3.4 keV of the energy deposition in the sample.

A sketch of the setup can be seen in Fig. 6.3. In a distance of 5 cm from the ^{137}Cs source a container filled with liquid scintillator is mounted. It is made of black high-density polyethylene, as it does not react with the scintillator. The container is of cylindrical shape with a diameter of 25 mm and a length of 20 mm. On both ends, it provides thick quartz glass windows that are 2mm strong. Via a small hole in the centre of the barrel of the container can be filled with liquid scintillator. It is sealed with a screw that has be enwrapped in Teflon tape in order to prevent oxygen getting into the container and reacting with the scintillator.

Opposed to the γ source a photomultiplier tube (PMT 9111B from Electron Tubes) collects the scintillation light emitted by the sample. The PMT has a plano-concave window that is 25 mm in diameter. This corresponds to the size of the window of the scintillator container. Only a small air gap is left between the glass window of the sample and the photocathode of the PMT. This setup ensures a high light collection efficiency. The PMT is
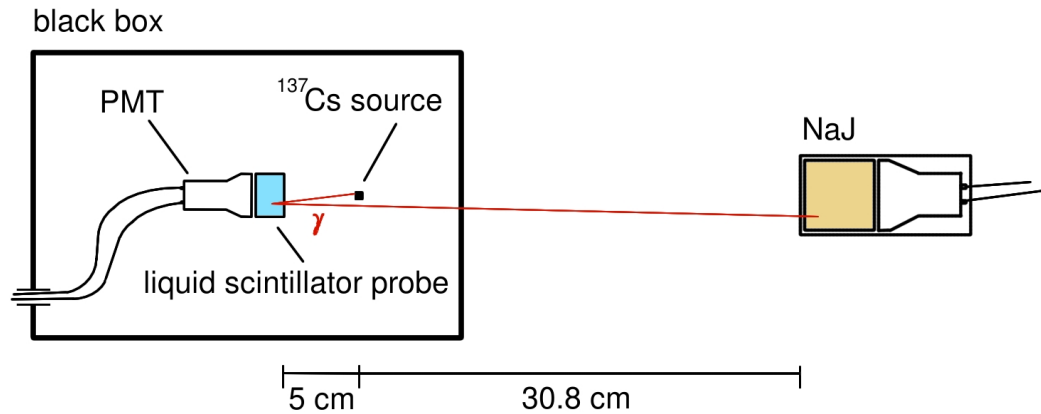
Figure 6.3: Schematic experimental setup. A γ emitted from the ^{137}Cs source is backscattered in the scintillator sample and detected in the NaJ counter. This way, a monoenergetic energy deposition in the scintillator is ensured. The scintillation light is detected by a PMT attached to the sample vessel.

shielded against external magnetic fields with a μ-metal foil surrounding its front part. Its spectral sensitivity covers a range from 280-630 nm [81].

PMT, scintillator container and ^{137}Cs source are installed in a black box in order to prevent external light to disturb the measurement. The small connector tube at one side of the box for both the high voltage supply and for the signal cable of the PMT has been light-tightened with black felt. A grounded aluminium sheet on top of the box minimizes electronic interferences. Lead sheets shield the surroundings from the γ-source inside. Furthermore, a blanket of black felt covers the setup as a whole.

In a distance of 30.8 cm from the γ source, a NaJ counter is positioned. This relatively large distance prevents a possible pile-up of γ events in the detector. Due to the photo peak detection, the NaJ scintillator crystal provides a very good energy resolution. The NaJ is cylindrical with a diameter of 7.5 cm and a length of 7.5 cm. It is sealed in an aluminium box to protect the crystal from external light and air moisture. The scintillation light from the NaJ is detected with another photomultiplier.

6.3   Electronics

For the readout electronics, NIM standard has been used. A block diagram of the electronics is shown in Figure 6.4.
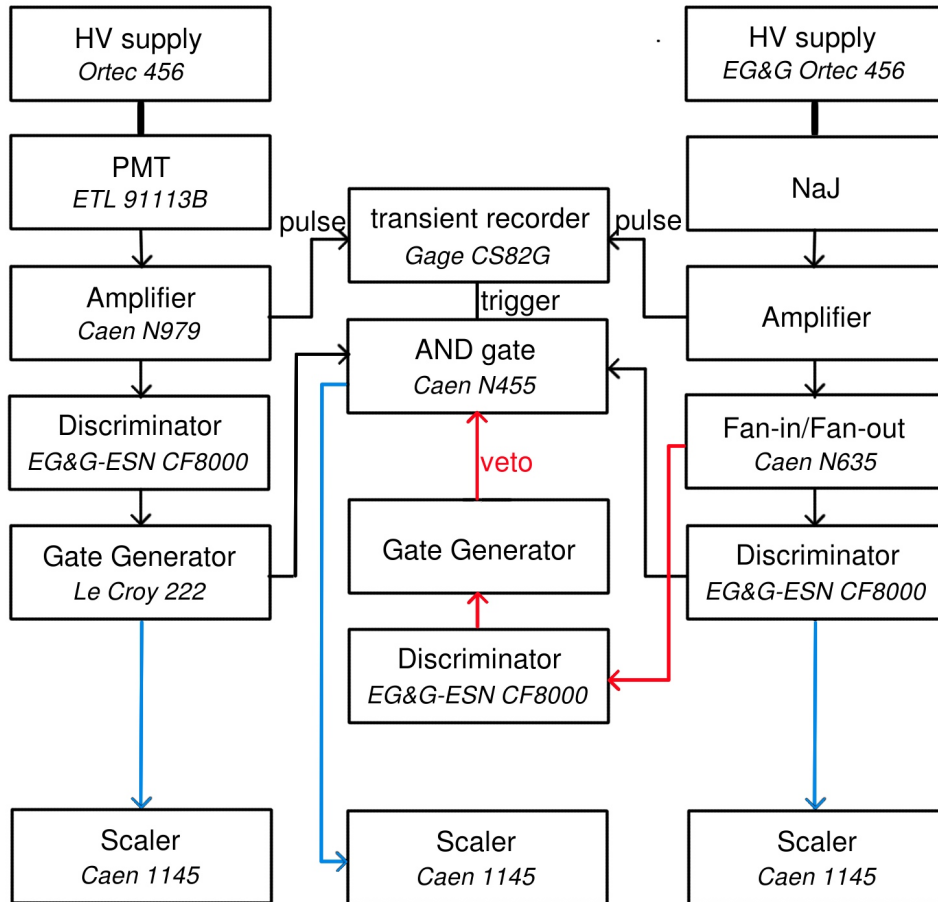
Figure 6.4: Block diagram of the readout electronics.

At a first stage, both the signals from PMT and NaJ are amplified. The PMT signal is then directly lead to a discriminator with a threshold of 100 mV (corresponding to ~300 keV) in order to suppress thermal dark noise.

The NaJ signal is forwarded to a Fan-in/Fan-out module where a second signal is branching off that will later serve as a veto for high energetic events. Both signals are sent to a discriminator, where the thresholds are set to 30 mV (90 keV) and 220 mV (660 keV) for the NaJ signal and the high energy veto signal, respectively.

Before the logical signals of PMT and NaJ can be combined in an AND gate, the PMT discriminator signal has to be delayed by 140 ns and broadened to 150 ns with the help of a gate generator in order to enable a coincidence. This is taking into regard the slow detector response of the NaJ in comparison to the fast system consisting of liquid scintillator and PMT.

When both PMT and NaJ see an event in coincidence, a trigger pulse is sent to a 10 bit transient recorder that reads out the amplified signals from NaJ and PMT. The maximal sampling rate is 250 MS†/s. In case the NaJ signal arose from a high energetic event, the veto signal described before is used to suppress this trigger pulse. The logic signal is broadened to 850 ns and is set in anti-coincidence to the trigger via the logic unit. However, due to a low rate the dead time is only $\sim 2 \cdot 10^{-5}$.

A scaler was used in order to monitor the coincidence rate and the rates from PMT and NaJ. While the NaJ showed throughout all measurements a constant rate of 1290 Hz, the rates in the scintillator seen in the PMT and the coincidence rate depended on the the liquid scintillator under investigation. The rates for the PMT varied between 460 Hz and 510 Hz, the coincidence rate between 1.3 Hz and 1.5 Hz. As the time window for a coincidence is 150 ns, random coincidences can be estimated to make up less than 6% of all events recorded. Correlated background might originate from multiple scatterings of γ's, for example on the lead sheets.

6.4   Analysis

The acquired events have been analysed using the Matlab software. The heights of the pulse maxima were taken as a measure of the energy deposition in both the scintillator and the NaJ. For each sample the pulse heights were plotted into a histogram providing an energy spectrum. As the energy of the backscattered γ's that are fully absorbed in the NaJ is expected to be around 184 keV, an additional software cut was applied on the NaJ spectrum between 144 keV and 245 keV. Events with more than one pulse in the sample have been rejected as well.

A spectrum of the liquid scintillator obtained with the PMT is shown in Figure 6.5. The background decreases exponentially with energy, while

---

†Megasample

the pulse height spectrum of the wanted backscattering coincidences shows a Gaussian distribution. For the analysis of the spectra, a fit was applied to the histogrammed pulse heights, considering background and signal:

$$N_{entr} = A \cdot \exp\left(\frac{-(x - x_0)^2}{2\sigma^2}\right) + B \cdot \exp\left(-kx\right). \qquad (6.2)$$

where x_0, the position of the maximum of the backscattering peak, is a measure of the light yield; σ is associated with the statistical error. Due to the high statistics of 30,000 events in one measurement (an analysis of the fits leads to an estimate, that $\sim$90% of them contribute to the backscattering peak) the statistical errors were very small, $\sim$0.2 %.
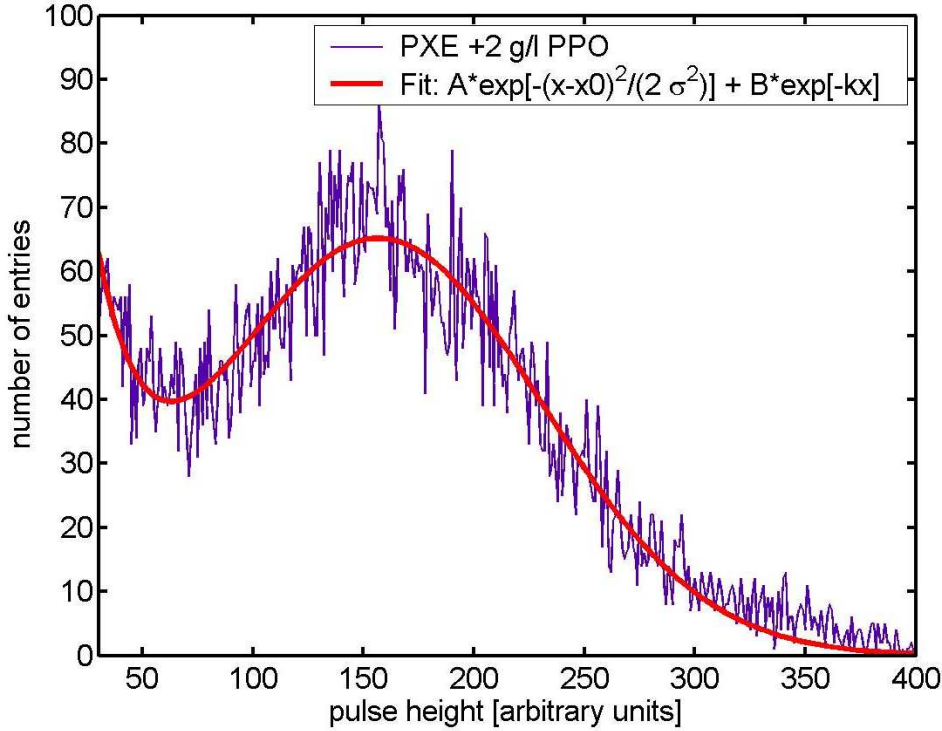
Figure 6.5: Pulse height spectrum of a coincidence measurement for the scintillator mixture PXE + 2 g/ℓ PPO. The fit considers both the Gaussian peak from the energy deposition of the backscattered γ's in the scintillator and the exponential background.

In order to get an estimation for the size of the statistical error, 3 independent coincidence measurements of the scintillator sample PXE + 2 g/ℓ PPO have been conducted. For each measurement, the container was first

emptied from the previous filling, disassembled and cleaned thoroughly with soap, water, and propanol. After the accurate reassembly, the container was filled with the new scintillator and put into the setup in the very same position as before in order to assure reproducibility. In order to prevent the PMT from being exposed to external light, it was disconnected from the high voltage supply during the installation. The coincidence measurement was started about one hour after the reconnection of the PMT to the voltage supply in order to maintain a stable PMT response, that could be monitored with the scaler.

For each measurement of the scintillator sample, the analysis described above was applied. The average of the differences of the pulse maxima of the backscattering peaks was taken as the measure of the systematical error. It is estimated to be about 3.3%.

Two separately mixed scintillator samples of PXE + 2 g/ℓ PPO have been investigated in the measurement. Thus, the systematical error represents to some extent the quality in which the mixture could be reproduced.

Another potential source for systematical errors is the cleanliness of the container. Although cleaned in several steps with water and propanol, it was difficult to keep the transparency of the glass windows the same during all measurements. The cleaning with wipes left behind small fibers that could never be totally removed, and might have induced scattering of the scintillation light.

Although the scintillator container was installed in the same manner every time, it was hardly manageable to get it into the exact same position every time. Already a small deviation from the parallelism of the glass windows of the container and the PMT might have a non-negligible impact on the number of collected photons due to light diffraction.

Both statistical and systematical error for all scintillator mixtures were calculated with Gaussian error propagation.

6.5   Results

Light yield measurements have already been conducted by M. Wurm for various types of scintillators [50]. However, both the solvent LAB and the fluor PMP have not been investigated closely, since the idea for their use in LENA

has emerged only recently. Overall, 6 mixtures have been regarded: PXE + 2 g/ℓ PPO for calibration, LAB + 2 g/ℓ PPO, PXE/LAB with 2 g/ℓ PMP, and PXE/LAB with 2 g/ℓ PPO + 20 mg/ℓ bisMSB. A fluor concentration of 2 g/ℓ for PPO and PMP has been chosen, since light yield of PXE + PPO nearly saturates at this level [50]. The results of the experiment are shown in Table 6.2.

scintillator mixture	light yield relative to PXE + 2 g/ℓ PPO		
PXE + PPO	100.0%	± 3.3% (syst.)	± 0.1% (stat.)
LAB + PPO	103.4%	± 3.1% (syst.)	± 0.2% (stat.)
PXE + PMP	79.1%	± 2.8% (syst.)	± 0.3% (stat.)
LAB + PMP	83.9%	± 2.8% (syst.)	± 0.2% (stat.)
PXE + PPO + bisMSB [1]	102.0%	± 3.0% (syst.)	± 0.3% (stat.)
LAB + PPO + bisMSB	99.7%	± 3.0% (syst.)	± 0.2% (stat.)

Table 6.2: Light Yield of different scintillator mixtures relative to PXE + 2 g/ℓ PPO.

From the measurements in the course of this thesis, two main results can be derived. First, independent from the fluor that has been added, PXE and LAB show the same light yield within the experimental uncertainties. Second, the light yield of both solvents with PMP is about 80 % of that with PPO in the same concentration. Once more, the difference of the light yields between PXE and LAB is not significant. The light yield might be smaller because of a less efficient energy transfer from the solvent to the fluor or energy loss processes of the fluor. Additionally, it is also affected by the spectral response curve of the PMT whose maximum is at 350 nm while PMP and PPO emit at 430 nm and 370 nm, respectively.

It is noteworthy that PPO emits around 400 nm where the attenuation length is smaller than at 430 nm, the emission of PMP. Due to the small scale of this experiment, this effect does not have an impact on the light yield measured in these two cases. However, since the LENA detector is supposed to have a diameter of ∼30 m, it cannot be neglected. Therefore, the light yield of PXE and LAB with PPO and bisMSB as fluors, emitting scintillation light around 430 nm like PMP, has been investigated as well. It is of the same order as the scintillator with PPO, giving proof that scattering

---

[1]data from M. Wurm [50]

and absorption in the liquid scintillator play a minor role at small scales.

As PXE and LAB showed equal light yields, mainly other physics parameters like attenuation length and scintillation decay times would determine a final choice between those two solvents. It is noteworthy, that in measurements for SNO+ [80], the effective light yield of LAB + 2 g/ℓ PPO was determined to be 90% of the light yield of PXE +2 g/ℓ PPO.

Chapter 7

Spatial Event Reconstruction

Spatial event reconstruction plays an important role in the LENA detector for the identification of delayed coincidence signals that happen almost at the same location in the detector if convection effects are low. It is also useful for the definition of a fiducial detector volume, as it allows discrimination of background due to intrinsic radioactivity and external radiation, e.g. muons and neutrons. Furthermore, spatial reconstruction can help to discriminate between two simultaneous events and to determine the energy deposition.

In order to quantitatively estimate the potential of spatial event reconstruction in the LENA detector, a Monte Carlo simulation has been performed. First, a high statistics data base has been created, storing the information on events at different locations inside the detector volume. The event location is reconstructed with a maximum likelihood method, comparing the hit pattern for each event with the database.

In the first section, the Monte Carlo simulation is introduced, i.e. the implemented physics processes and the detector geometry. The analysis of the simulated data is explained in the second section, and the results of the spatial reconstruction are explained in the last section.

7.1 Monte Carlo Simulations with Geant4

Geant4 is a C++ based toolkit for simulations in particle physics [82, 83]. It is a tool for the generation, tracking and detection of particles. Originally, the software has been designed for applications in high energy, nuclear and accelerator physics, but due to the wide range of physical processes included it is also applicable in many other areas.

The simulation program in use is based on a former program designed for the LENA detector by T. Marrodán Undagoitia [84]. Considering scintillation physics, it includes scintillation decay times, Čerenkov light production, quenching effects, Rayleigh scattering and light absoption. The input parameters have been determined in experiments for Borexino [11] and experiments by M. Wurm at Garching [50].

The input parameters for the simulation were a light yield of 10,000 photons per MeV, a PMT efficiency of 20% and scattering and absorption lengths of 20 m. The scintillation decay times have been set to 3.4 ns and 17 ns. The detector is assumed to be filled with PXE.

In order to use the simulation for spatial reconstruction, an additional class has been implemented in the original code. It is responsible for the positioning of the photomultipliers (PMTs) and the simulation of their response, including a Gaussian time jitter of 1 ns and an imprecision of charge collection (Gaussian with a width of ≈ 0.24 photo electons [85]). This has been done in a flexible way, allowing to specify the number and size of the PMTs at will while the new class will guarantee a uniform distribution of the PMTs all over the detector. The PMTs are represented by flat, circular-shaped areas and are numbered continuously. In the readout class, only these areas have been set to be sensitive to photons. For each photon hitting a PMT, information on the time and the number of the PMT is stored. Figure 7.1 shows a histogram with all data that is saved to disk.

Figures 7.2 and 7.3 show the setup of the cylindrical-shaped detector used in simulations for the spatial reconstruction from the side and head-on. Overall, more than 13,000 PMTs with a diameter of 50 cm ensure a coverage of 30%. The active areas of the PMTs are all positioned in a distance of 0.5 m from the edge of the cylindrical-shaped, inner vessel. On the cylinder barrel, the PMTs are aligned in 120 rings with 100 photomultipliers each; on the bases they are aligned in rings around one PMT in the very center, resulting in 841 PMTs in total.

The simulation has been performed for electrons at energies of 1 and 10 MeV. In this energy range, the events can be considered to be point-like sources of scintillation light as the track length at 10 MeV is about 1 cm. In addition, the hit patterns induced by such events can be easily scaled to intermediate and higher energies as long as the track length remains negligible in comparison to the spatial resolution of the detector.
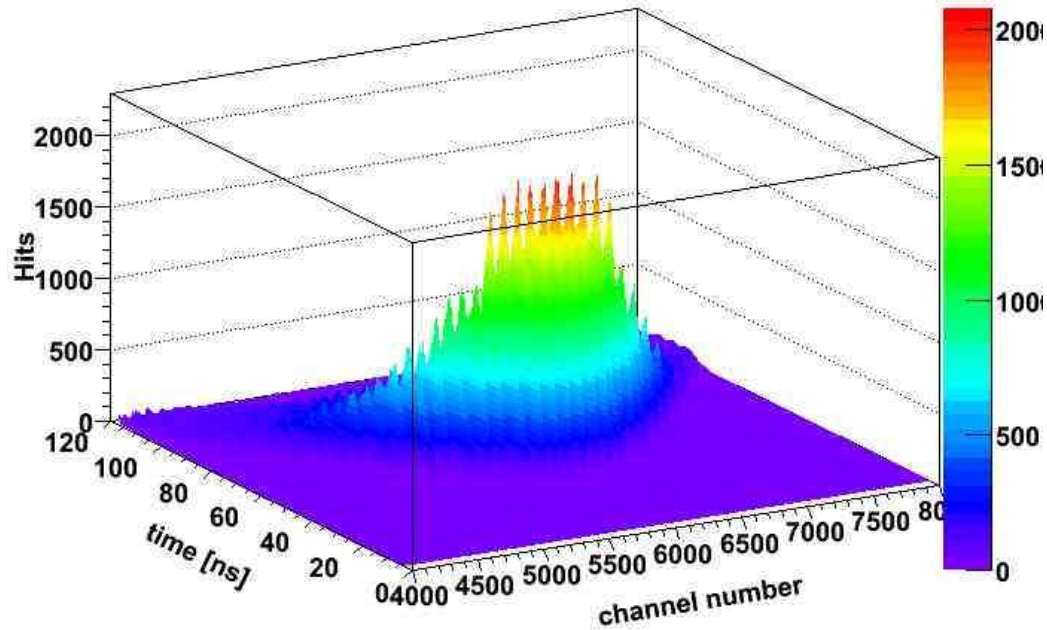
Figure 7.1: Number of hits in dependence on the PMT number and the hit time. The histogram includes the result of 2000 simulated events of 10 MeV electrons at 4 m radially from the centre. The first photons reach the PMTs after ~ 43 ns after the generation of the particle. The "finger" structure results from the alignment in rings (and the corresponding numbering) of the PMTs on the cylinder barrel. As 100 PMTs form a ring, the distance between 2 peaks is 100 in the numbering of the channels.

The position of the events were chosen at different radii and axial distances from the centre in order to test both radial and axial resolution of the detector.

7.2 Data Analysis with ROOT

The output of the simulation was analysed with ROOT, an object oriented framework developed at CERN [86]. The simulation data has been saved in a ROOT tree, a format that provides efficient processing. The analysis has been performed with C++ based macros.
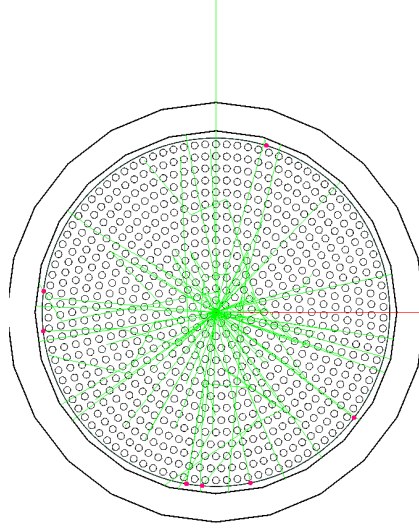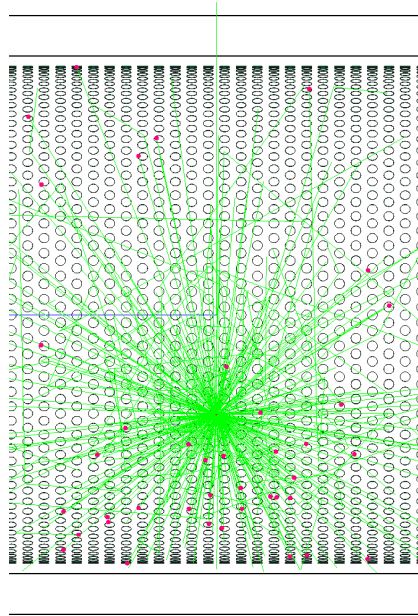
Figure 7.2: Head-on view of the detector setup implemented in the simulation. The photomultipliers are illustrated as circles, photon tracks from the scintillation light are shown in green and PMT hits are marked with red dots. The perpendicular green and red line represent y- and x-axis, respectively.

The basic idea behind the spatial reconstruction code is the comparison of the hit pattern of an event with the hit patterns of events at known positions stored in a database. The comparison is done with a maximum likelihood analysis. For those photomultipliers that have a non-zero entry of hits in the database, the probability is computed that they detect the number of photons simulated for the single event.

The probability p_i that the i-th PMT registers k_i photoelectrons from scintillation light emitted at the place r follows a Poisson distribution:

$$p_i(k_i|r) = \frac{\mu_i^{k_i}}{k_i!}e^{-\mu_i} \tag{7.1}$$

where μ_i is the mean number of hits the i-th PMT registers for an event at r. The data for the μ_i are taken from the simulations of 2000 events for each position. After a normalisation, an independent simulation of a single event is compared to the hit patterns that have been stored in look-up tables.

The likelihood function $\mathcal{L}(r)$ can be written as

$$\mathcal{L}(r) = \prod_{i=1}^{N_{PMT}} p_i(k_i|r). \tag{7.2}$$

Figure 7.3: View from the side on a part of the detector as implemented in the simulation. The photomultipliers are illustrated as circles, photon tracks from the scintillation light are shown in green. Photomultiplier hits are marked with red dots. The perpendicular green and blue line represent y- and z-axis, respectively.

The product considers all photomultipliers N_{PMT} that registered an event stored in the look-up table. The maximum of the likelihood function is the best estimate for the event location. For high statistics, the likelihood function follows a Gaussian distribution.

In general, it is easier to calculate the logarithm of the likelihood function,

$$ln\mathcal{L}(r) = \sum_{i=1}^{N_{Hits}} ln(p_i(k_i|r)) = \sum_{i=1}^{N_{Hits}} (-\mu_i + k_i\mu_i + ln(k_i!)), \qquad (7.3)$$

and solving

$$\frac{dln\mathcal{L}(r)}{dr} = 0 \qquad (7.4)$$

in order to obtain the best estimate $\hat{r}$.

In the limit of large numbers, the error of the estimate can be calculated as

$$\sigma^2(\hat{r}) = -\left(\frac{d^2 ln\mathcal{L}(r)}{dr^2}\right)^{-1}. \tag{7.5}$$

7.3 First Results

In the analysis, the energy deposition and the angle in the plane perpendicular to the axis of the cylinder were considered as known. In practice, the likelihood function is only known for some radii r_j, where high statistics simulations have been performed and stored in a look-up table. As mentioned, the likelihood function follows a Gaussian distribution for high statistics. Thus, the logarithm of the likelihood function can be fitted with

$$ln\mathcal{L}(r) = -\frac{(x-x_0)^2}{\sigma^2} + c. \tag{7.6}$$

According to Eq. (7.5), the error of the estimate and therefore the uncertainty in the reconstruction of the event is equal to σ. Figure 7.4 shows a plot of the logarithm of the likelihood function in dependency on the radius of the detector for an energy deposition of 10 MeV. According to Eq. (7.6), a fit has been applied to the $ln\mathcal{L}$ considering the data around the maximum. The event can be reconstructed with an uncertainty of 18 cm (1 standard deviation).

Figure 7.5 shows the dependency of σ on the radius of the event for energy depositions of 1 MeV and 10 MeV. Events at higher energies are more easily to reconstruct, as more photons are created and thus higher statistics are obtained. Moreover, events closer to the PMTs are reconstructed more precisely as more photons are detected.

Figure 7.6 shows the behaviour of the uncertainty of the reconstructed spatial position in dependence on the energy deposition. The error is inversely proportional to the square root of the number of photons detected in the event. As this number is proportional to the energy deposition, the energy dependency of the error σ is

$$\sigma(E) = \frac{\eta}{\sqrt{E}}, \tag{7.7}$$

where η is a constant that can be obtained with a fit applied at the data. The quality of the reconstructed position increases for higher energy depositions in the scintillator. As an example, Figure 7.6 shows a fit to simulated data for events at a radius of 10 m, well reproducing the inverse square-root law.
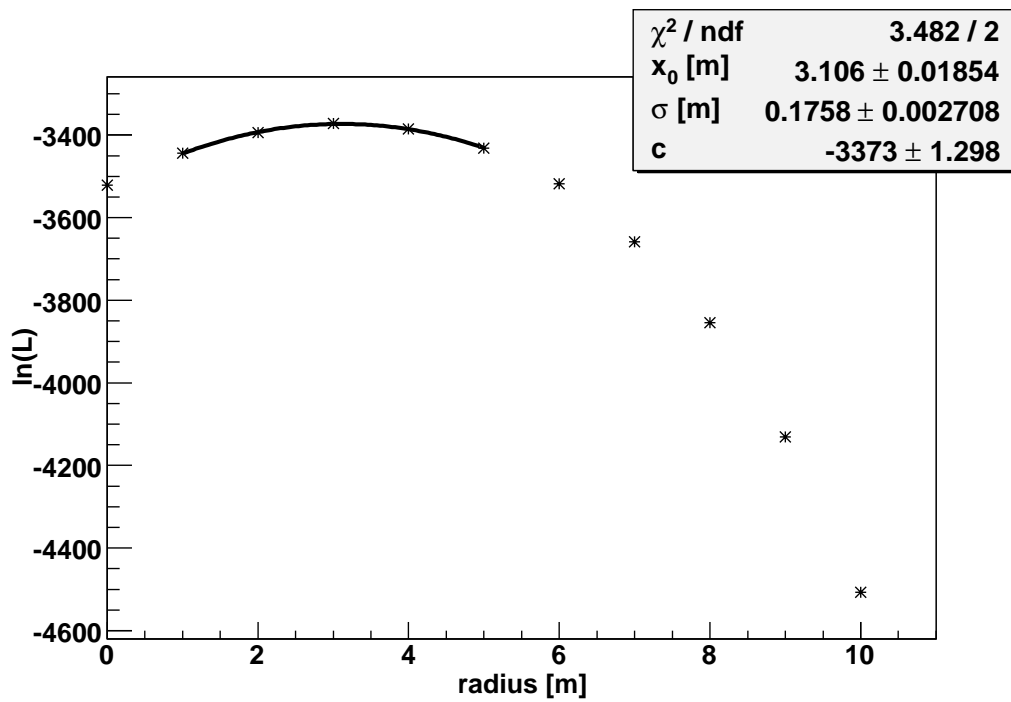
Figure 7.4: For a simulated event at $r = 3$ m, $\ln \mathcal{L}$ is plotted versus the radius. A fit according to Eq. (7.6) has been applied around the maximum bin. A resolution σ of ~ 18 cm is obtained.
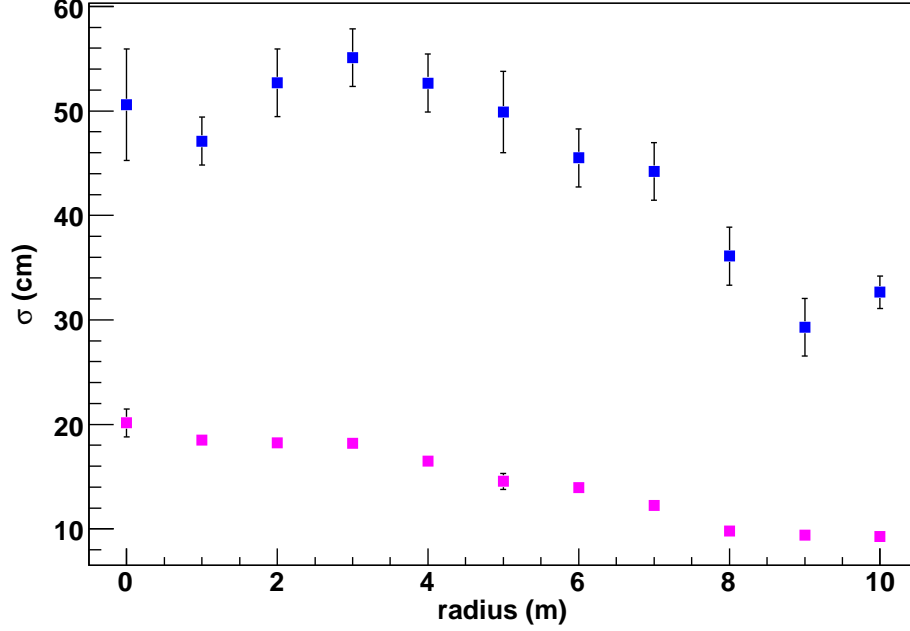
Figure 7.5: Uncertainty σ in the reconstructed radial event position as a function of the radius for events of 1 MeV (blue) and 10 MeV (red). Notice that σ decreases with the deposed energy and with distance from the centre. This effect is due to the increase in detected photons and therefore in statistics.

The data for events at other radii show the same dependency on the energy.

The axial resolution obtained in the same manner is about 25 cm, due to a larger distance between the simulated grid points. However, using more reference points, it should be possible to obtain a resolution of $\sim$20 cm, comparable to the result of the radial uncertainty of the reconstruction in the very centre. The axial resolution of a parallely shifted line with respect to the axis of the cylinder should increase for smaller distances to the PMTs, due to higher statistics.

The presented method of spatial reconstruction works very well for energies around 10 MeV. While the location can be determined with an accuracy of 10 cm for an event 10 m from the centre of the detector, the uncertainty of an event in the center is $\sim$ 20 cm. However, for low energetic events, as for solar neutrinos and for a part of the SN-ν spectrum, the technique of
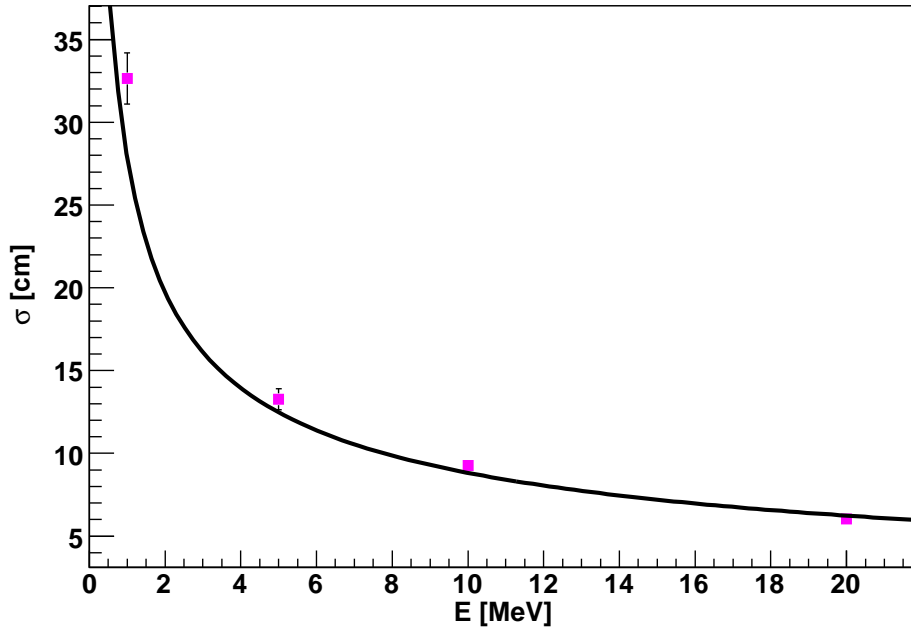
Figure 7.6: Uncertainty σ of the reconstructed event position in dependency on the energy deposition in the scintillator at a radial position of 10 m. The error decreases with increasing energy according to Eq. (7.7).

relying only on the spatial photon hit pattern will not be sufficient to obtain a resolution of this order. In this case, taking advantage of the knowledge of the PMT hit times might fuerther improve the reconstruction, as shown in investigations for the CTF for Borexino [87]. Preliminary studies however showed, that for the large amount of data to be stored in a database and to be recalled upon every event, the computation times for the spatial reconstruction increase immensely. Therefore, the spatial reconstruction program should be designed in a way, that in a first step fast algortihms reduce the number of PMTs that have to be considered for the last, while a second step uses both space and time information on the PMT hits for the calculation of the event location.

A fast and possible method to confine a smaller volume within the detector is to consider the sum of hits for each PMT ring only, as shown in Figure 7.7. Determining the maximum and setting a window around can help to decrease the number of PMTs that have to be considered in a subsequent and more precise spatial reconstruction algorithm.
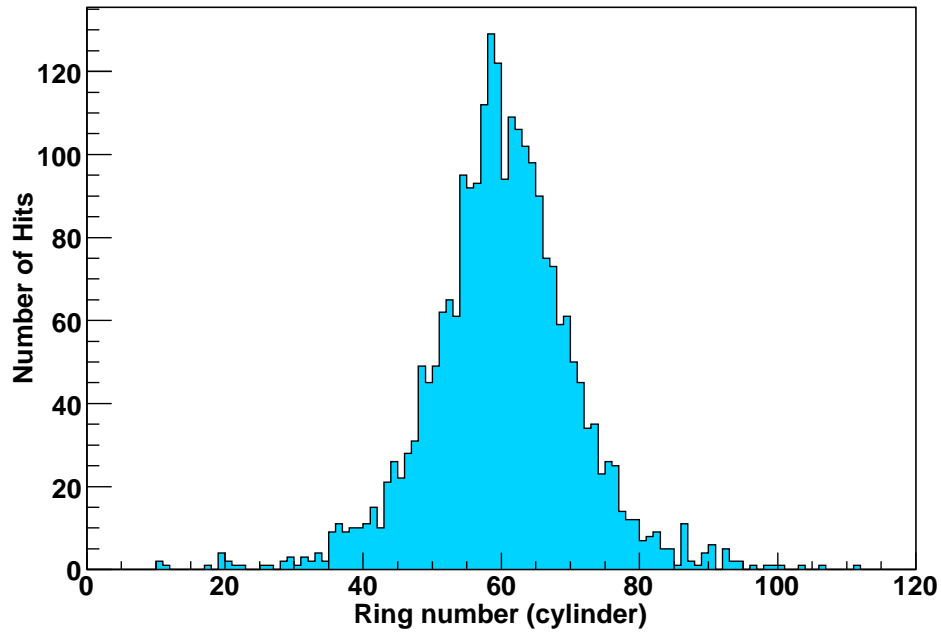
Figure 7.7: Histogram of hits summed up for all PMTs in one ring on the cylinder barrel. The application of cuts around the maximum in order to consider only rings exceeding a defined number of hits could be a fast algorithm to confine a smaller detector volume.

Chapter 8

Conclusions and Outlook

The main part of this thesis has been dedicated to the possible observation of neutrinos from a galactic core-collapse supernova in LENA. Overall, eight sensitive reactions for SN-ν (four neutral current and four charged current reactions) have been presented along with their signatures. Moreover, the event rates of these reaction channels were investigated for the three most common SN models and dependent on the oscillation scenario. The total event rate, considering a 8 $M_\odot$ SN in the centre of our galaxy, varies between $1 - 2 \cdot 10^4$. The channels with the highest statistics are the inverse beta decay with ~6,000-11,000 events, the NC scattering on Carbon with ~700-2,000 events, and the elastic scattering on protons with ~600-5,700 events. However, the last channel is sensitive on the energy threshold of LENA. Independently from the oscillation scenario, the neutral current channels provide information on the total neutrino flux and thus allow a distinction between the different SN models. The charged current channels allow spectroscopy and flux measurement of ν_e and $\overline{\nu}_e$. Information on the original $\overset{(\,)}{\nu}_x$-flux $(x = \mu, \tau)$ can be obtained with the elastic scattering on protons, as it is very selective on high-energetic neutrinos due to its high detection threshold, and as the average energy of $\overset{(\,)}{\nu}_x$ is higher compared to electron-type neutrinos.

The impact of the neutrino mass hierarchy and the size of θ_{13} on the single channels via resonance effects in the SN and transition through the Earth has been discussed thoroughly. With the comparison of the different channel event rates, a distinction between the individual resonance scenarios might be feasible in LENA. Another possibility to gain information on oscillations is the observation/non-observation of the neutronisation burst, especially in the channels sensitive to ν_e, where overall ~70 events are expected. A possible observation of the Earth Effect in the inverse beta decay

channel in LENA has been discussed qualitatively showing that, for small θ_{13}, it offers a unique chance to determine this last unknown mixing angle. In the future, a quantitative investigation on the detection sensitivity of LENA should therefore be considered. A further issue are supernova shock waves that are expected to have a characteristic impact on the neutrino spectra, allowing further conclusions on the SN explosion mechanism.

In an experimental part of this work, the effective light yield of possible organic liquid scintillators for LENA has been measured. The light yield is a quantity largely affecting the energy and the spatial resolution of the detector, which are relevant for ν spectroscopy and the discrimination of different channels. In the quest for an optimal liquid scintillator for LENA, the solvent LAB and the wavelength shifter PMP, both considered only recently for a possible application in LENA, were in the centre of the investigations. While the light output of LAB with any fluor was a good as the default scintillator based on PXE, liquid scintillator mixtures with PMP showed a reduction of 20% in the light yield.
The decision which scintillator is most appropriate for LENA regarding its requirements is dependent on the outcome of the current experiments on the scintillation decay times and the attenution length.

Several SN-ν detection reactions feature a delayed coincidence signal as event signature. Spatial reconstruction is vital for the identification of these events. With the help of a MC simulation and the application of a maximum likelihood calculation using the PMT hit patterns, it was shown that a radial resolution of 20 cm and 50 cm can be easily achieved for events of 10 MeV and 1 MeV, respectively.
A more precise algorithm could compare the hit patterns of the PMTs for each time bin. However, computing time would increase immensely due to the large number of PMTs in LENA. This problem could be solved applying pre-algorithms that already confine a smaller volume within the whole detector. For example in a first step, one could take advantage of the circular alignment of the PMTs and select a slice of the cylinder of the LENA detector, before confining the volume further applying the maximum likelihood analysis developed in this thesis. An interesting task will be the reconstruction of events close to the cylinder bases, i.e. with regard to the number of PMTs necessary for a sufficient spatial resolution.

The success of the liquid-scintillator experiments Borexino [11] and Kam-LAND [17, 18] greatly motivates to keep on developing a large-scale detector as LENA. While having benefits from their experience, further investigations

have still to be done concerning both technical issues and phenomenology as LENA covers a wider range of physics. Scintillation decay times, attenuation length, and emission and absorption spectra of different liquid scintillators are currently under inverstigations. Detector simulations and experiments on the liquid scintillator advance hand in hand in order to make predictions on the performance of the detector. For instance, further proton decay studies require codes for the reconstruction of tracks.

Bibliography

[1] R. Davis, Prog. Part. Nucl. Phys. **32**, 13 (1994).

[2] K. Hirata *et al.*, Phys. Rev. Lett. **58**, 1490 (1987).

[3] K. Hirata *et al.*, Phys. Rev. D **38**, 448 (1988).

[4] R.M. Bionta *et al.*, Phys. Rev. Lett. **58**, 1494 (1987).

[5] C.B. Bratton *et al.*, Phys. Rev. D **37**, 3361 (1988).

[6] M. Boulay *et al.*, Phys. Rev. Lett. **89**, 011301 (2002).

[7] GNO collaboration, M. Altmann *et al.*, Phys. Lett. B **616**, 174 (2005).

[8] GALLEX collaboration, P. Anselmann *et al.*, Phys. Lett. B **357** 237 (1995).

[9] J.N. Abdurashitov *et al.*, J. Exp. Theor. Phys. **95**, 181 (2002).

[10] Super-Kamiokande Collaboration, J. Hosaka *et el.*, Phys. Rev. D **73**, 112001 (2006).

[11] Borexino Collaboration, C. Arpesella *et al.*, arXiv:astro-ph/07082251 (2007).

[12] C. Lunardini, arXiv:astro-ph/0610534 (2006).

[13] M.S. Malek *et al.* (Super-Kamiokande Collaboration), Phys Rev. Lett. **90**, 061101 (2003).

[14] The BAIKAL collaboration, Zh.-A. Dzhilkibae *et al.*, arXiv:astro-ph/0609711 (2006).

[15] Amanda collaboration, M. Ackermann *et al.*, Phys. Rev. D **71**, 077102 (2005).

[16] Super-Kamiokande Collaboration, Y. Ashie *et al.*, arXiv:hep-ex/0501064 (2005).

[17] The KamLAND collaboration, T. Karaki *et al.*, Nature **436**, 499 (2005).

[18] K. Eguchi *et al.*, Phys. Rev. Lett. **90**, 021802 (2003).

[19] The CHOOZ collaboration, M. Apollonio *et al.*, Eur. Phys. J. **C27**, 331 (2003).

[20] The K2K collaboration, M. H. Ahn *et al.*, Phys. Rev. D **74**, 072003 (2006).

[21] Minos Collaboration, arXiv:hep-ex/0708.1495 (2007).

[22] E.D. Church *et al.*, Phys. Rev. D **66**, 013001 (2002).

[23] The MiniBooNE collaboration, A. A. Aguilar-Arevalo *et al.*, Phys. Rev. Lett. **98**, 231801 (2007).

[24] K. Nakamura, Int.J. of Mod. Phys. A **18**, 22 (2003).

[25] A. de Bellefon *et al.*, arXiv:hep-ex/0607026 (2006).

[26] UNO EOI and R&D Proposal , http://ale.physics.sunysb.edu/uno/publications/uno-rnd-proposal05-DOE_111105.pdf (2005).

[27] A. Ereditato and A. Rubbia, Nucl. Phys. Proc. Suppl. **154**, 163 (2006).

[28] A. Ereditato and A. Rubbia, Nucl. Phys. Proc. Suppl. **155**, 233 (2006).

[29] SNO collaboration, Letter of Intent, http://www.snoplus.phy.queensu.ca/LOI.pdf (2004).

[30] HanoHano collaboration, http://www.phys.hawaii.edu/ jgl/hanohano.html.

[31] L. Oberauer *et al.*, Nucl. Phys. Proc. Suppl. **138**, 108 (2005).

[32] T. Marrodán Undagoitia *et al.*, Prog. Part. Nucl. Phys. **57**, 283 (2006).

[33] K.A. Hochmuth *et al.*, Astropart. Phys. **27**, 21 (2007).

[34] T. Marrodán Undagoitia *et al.*, Phys. Rev. D **72**, 075014 (2005).

[35] M. Wurm *et al.*, Phys. Rev. D **75**, 023007 (2007).

[36] The LAGUNA collaboration, D. Autiero *et al.*, arXiv:hep-ph/0705.0116 (2007).

[37] A.G. Lyne *et al.*, Mon. Not. R. astr. Soc. **295**, 743 (1998).

[38] G.A. Tammann, Astron. Astrophys. **8**, 458 (1970).

[39] S. Ando, K. Sato, and T. Totani, Astropart. Phys. **18**, 307 (2003).

[40] T. Totani *et al.*, ApJ **496**, 216 (1998).

[41] M.Th. Keil *et al.*, ApJ **590**, 971 (2003).

[42] T.A. Thompson *et al.*, ApJ **592**, 434 (2003).

[43] S.P.Mikheyev and A. Yu Smirnov, Sov. J. Nucl. Phys. **42**, 913 (1985).

[44] L. Wolfenstein, Phys. Rev. D **17**, 2369 (1978).

[45] E. Kh. Akhmedov, S. T. Petkov, and A. Yu Smirnov, Phys. Rev. D **48**, 2167 (1993).

[46] K. Kobayashi *et al.*, Phys. Rev. D **72**, 052007 (2005).

[47] T. Hakaya, Nucl. Phys. B, Proc. Suppl. **138**, 376 (2005).

[48] S. Raby, talk presented at SUSY'02, DESY, Hamburg, Germany (2002).

[49] M. Lindner, "XXth International Conference on Neutrino Physics and Astrophysics", Munich, Germany (2002), Springer Tracts Mod. Phys. **190**, 209 (2003).

[50] M.Wurm, "Untersuchungen zu den optischen Eigenschaften eines auf PXE basierenden Flüssigszintillators und zum Nachweis von 'Supernova Relic Neutrinos' mit dem zukünftigen Neutrinodetektor LENA", Diploma Thesis, Technical University Munich (2005).

[51] Freedman, Roger A.: Universe, W.H. Freeman and Company, New York, 2005.

[52] S.A. Colgate, R.H. White, ApJ **143**, 626 (1966).

[53] J.R. Wilson, Numerical Astrophysics (Boston:Jones & Barlett) (1985).

[54] M. Liebendörfer *et al.*, Astrophys. J. Suppl. **150**, 263 (2004).

[55] K. Kotake *et al.*, arXiv:astro-ph/0509456v2 (2005).

[56] Schmitz, Norbert: Neutrinophysik. Teubner Studienbcher, Stuttgart, 1997.

[57] Particle Physics Booklet, extracted from W.-M. Yao *et al.*, Journal of Physics G **33**, 1 (2006).

[58] B. Aharmim *et al.*, Phys. Rev. C **72**, 055502 (2005).

[59] A.S. Dighe and A.Yu. Smirnov, Phys. Rev. D **62**, 033007 (2000).

[60] S. Skadhauge and R. Zukanovich Funchal, arXiv:hep-ph/0611194 (2006).

[61] C. Lunardini and A. Yu. Smirnov, JCAP **0306**, 009 (2003).

[62] R. Tomas *et al.*, JCAP **0409**, 015 (2004).

[63] A. Dighe *et al.*, arXiv:hep-ph/0304150 (2003).

[64] L. Cadonati *et al.*, Astroparticle Physics **16**, 361 (2002).

[65] M. Fukugita *et al.*, Phys. Lett. B **212**, 139 (1988).

[66] M. Fukugita *et al.*, Phys. Rev. C **41**, 1359 (1990)

[67] A.Ianni *et al.*, Phys. Lett. B **627**, 38 (2005).

[68] J.F. Beacom *et al.*, arXiv:hep-ph/0205220 (2002).

[69] S. Weinberg, Phys. Rev. D **5**, 1412 (1972).

[70] L.A. Ahrens *et al.*, Phys. Rev. D **35**, 785 (1987).

[71] C.H. Llewellyn Smith, Phys. Rept **3**, 261 (1972).

[72] S.M. Bilenky and J. Hosek, Phys. Rept **90**, 73 (1982).

[73] J.B. Birks, "The Theory and Practice of Scintillation Counting", Pergamon Press , London (1964).

[74] G. Alimonti *et al.*, Astropart. Phys. **16**, 205 (2002).

[75] Double-CHOOZ collaboration, F. Ardellier *et al.*, arXiv:hep-ex/0405032 (2004).

[76] Daya Bay collaboration, arXiv:hep-ex/0701029 (2007).

[77] P. Pfahler, "Bestimmung der absoluten Lichtausbeute des Flüssigszintillators für die äußeren Detektorkomponenten des Neutrinoexperiments Double Chooz", Diploma Thesis, Technical University Munich (2007)

[78] Borexino collaboration, S. Schönert *et al.*, arXiv:physics/0408032 (2004)

[79] C. Buck *et al.*, epoc.mpg.de/207303.

[80] M. Chen, "Scintillator Purification for SNO+", LRT2006, Aussois, France, http://lrt2006.in2p3.fr/talks/Chen_SNO+_Scint_Purif.pdf.

[81] Electron Tubes Ltd., 25 mm (1") photomultiplier 9111B series data sheet, http://www.electrontubes.com/pdf/9111B.pdf.

[82] G. Agostinelli *et al.*, Nucl. Instr. Meth. A **506**, 250 (2003).

[83] J. Allison *et al.*, Nuclear Science **53**, 270 (2006).

[84] T. Marrodán Undagoitia, "Search for the Proton Decay in the large liquid Scintillator Detector LENA", Diploma Thesis, Technical University Munich (2005).

[85] T. Marrodán Undagoitia, private communications.

[86] R. Brun and F. Rademakers, Linux Journal **51** (1998) and http://root.cern.ch/.

[87] M. Göger-Neff, Development of a Liquid Scintillator and of Data Analysis Methods for BOREXINO", PhD Thesis, Technical University Munich (2001).

Acknowledgements

Bauteilen wesentlich zum Gelingen des Experiment beigetragen haben.

Ein herzliches Dankeschön geht an Robert Hölzel, der sich nicht nur beim Korrekturlesen dieser Diplomarbeit verdient gemacht hat, sondern auch an einer sehr schönen, gemeinsamen Studienzeit.

Ein Dank gebührt meinen Geschwistern Angelika und Stefan für so ziemlich vieles, aber in diesem Fall vor allem für das Aufzeigen und das Voranschreiten auf einer wissenschaftlich Laufbahn.

Mein größter Dank gilt meinen Eltern, auf deren geistige, moralische und finanzielle Unterstützung ich mich während meiner gesamten Ausbildungszeit immer bedingungslos verlassen konnte, und ohne die ich mir bedeutend weniger Unsinn hätte leisten können.